1 **ORP5 TRANSFERS PHOSPHATIDYLSERINE TO MITOCHONDRIA AND**

2 **REGULATES MITOCHONDRIAL CALCIUM UPTAKE AT ENDOPLASMIC**

3 **RETICULUM - MITOCHONDRIA CONTACT SITES**

4

5 **Leila Rochin[1], Cécile Sauvanet[1]*, Eeva Jääskeläinen[2]*, Audrey Houcine[3]*, Amita**

6 **Arora[2], Annukka M. Kivelä[2], Xingjie MA[5,10], Eyra Marien[4], Jonas Dehairs[4],**

7 **Romain Le Bars[6], Julie Neveu[1], Elena Santonico[7], Johannes V. Swinnen[4], David**

8 **Bernard[5], David Tareste[8], Vesa M. Olkkonen[2,9], and Francesca Giordano[1#]**

9

10 [1] Institute for Integrative Biology of the Cell (I2BC), CEA, CNRS, Univ. Paris-Sud,

11 Université Paris-Saclay, Gif-sur-Yvette cedex 91198, France.

12 [2] Minerva Foundation Institute for Medical Research, Biomedicum 2U, FI-00290

13 Helsinki, Finland

14 [3] Institut Jacques Monod, CNRS, UMR7592, Université Paris Diderot, Sorbonne

15 Paris Cité, F-75013 Paris, France

16 [4] Laboratory of Lipid Metabolism and Cancer, Department of Oncology, KU Leuven,

17 Leuven B-3000, Belgium.

18 [5] Centre de Recherche en Cancérologie de Lyon, UMR INSERM U1052/CNRS 5286,

19 Centre Léon Bérard, 69373 LYON Cedex 08, France

20 [6] Imagerie-Gif, Light Microscopy Facility, Institute for Integrative Biology of the Cell

21 (I2BC), CEA, CNRS, Univ. Paris-Sud, Université Paris-Saclay, Gif-sur-Yvette cedex

22 91198, France

23 [7] University of Rome Tor Vergata, via della ricerca scientifica, dipartimento di

24 Biologia, 00133, Italy

25   [8] Institute of Psychiatry and Neuroscience of Paris (IPNP), UMR-S1266 INSERM-

26   Paris Descartes University, Paris, France

27   [9] Department of Anatomy, Faculty of Medicine, FI-00014 University of Helsinki,

28   Finland

29   [10] Xingjie MA present address: The Affiliated Hospital of Yangzhou University,

30   Yangzhou University, Yangzhou, China

31

32

33   * These authors contributed equally to this work

34   # Correspondence to: francesca.giordano@i2bc.paris-saclay.fr

35

SUMMARY

Mitochondria are dynamic organelles essential for cell survival whose structural and functional integrity rely on selective and regulated transport of lipids from/to the endoplasmic reticulum (ER) and across the two mitochondrial membranes. As they are not connected by vesicular transport, the exchange of lipids between ER and mitochondria occurs at sites of close organelle apposition called membrane contact sites. However, the mechanisms and proteins involved in these processes are only beginning to emerge. Here, we show that ORP5/8 mediate non-vesicular transport of Phosphatidylserine (PS) from the ER to mitochondria in mammalian cells. We also show that ER-mitochondria contacts where ORP5/8 reside are physically and functionally linked to the MIB/MICOS complexes that bridge the mitochondrial membranes, cooperating with them to facilitate PS transfer from the ER to the mitochondria. Finally, we show that ORP5 but not ORP8, additionally regulates import of calcium to mitochondria and consequently cell senescence.

50

51   **KEYWORDS**

52   Membrane contact sites, mitochondria, ORP, lipid transfer, calcium

53

54   **INTRODUCTION**

55   Vesicular trafficking is the major pathway for transport of proteins and metabolites,

56   such as lipids, between membranes. However, an alternative route, which is vesicle-

57   independent, occurs at regions of close inter-organelle membrane proximity (within less

58   than 30 nm) also called membrane contact sites (Scorrano, De Matteis et al., 2019).

59   This route is particularly important to preserve membrane composition, integrity and

60   identity of the intracellular organelles such as the mitochondria that are largely excluded

61   from the classical vesicle-mediated trafficking pathways. Like other organelles,

62   mitochondria can be closely associated with the endoplasmic reticulum (ER), the major

63   site of lipid synthesis and the major intracellular calcium (Ca^{2+}) store. ER membrane

64   subdomains closely apposed to the mitochondria are called mitochondria-associated ER

65   membranes (MAMs) and they facilitate the exchange of Ca^{2+} and lipids between the two

66   organelles (Herrera-Cruz & Simmen, 2017, Tatsuta, Scharwey et al., 2014, Vance,

67   2014)

68   Mitochondria are involved in a plethora of cellular processes including energy

69   production, lipid metabolism, Ca^{2+} homeostasis and apoptosis. To fulfill their numerous

70   functions, mitochondria need to maintain a defined membrane composition by receiving

71   essential lipids and lipid precursors from the ER through membrane contact sites

72   (Giordano, 2018, Vance & Tasseva, 2013).

73   Increasing lines of evidence suggest that lipid transfer proteins (LTPs) play a major

74   role in regulating the lipid composition of membranous organelles by facilitating non-

3

75   vesicular lipid transport at membrane contact sites. In recent years, several tethering

76   complexes with lipid transfer activity have been identified at membrane contact sites

77   between the ER and other intracellular organelles including the plasma membrane (PM)

78   in yeast as well as in mammalian cells. However, our knowledge of how lipids are

79   exchanged at ER-mitochondria membrane contact sites remains still rudimentary, and

80   the LTPs that localize and function at these sites are largely unknown. The best-studied

81   lipid transfer/tethering complex at ER-mitochondria contact sites is the yeast ER-

82   mitochondria encounter structure (ERMES) (Kornmann et al 2009, Lang et al 2015) that

83   bridges the ER and the mitochondrial membranes and also facilitates the exchange

84   of phospholipids (in particular phosphatidylcholine, PC) between them. In metazoans,

85   very little is known on how lipids are exchanged at ER-mitochondria membrane

86   contact sites and about the proteins involved in this process. Some tethers at

87   mammalian ER-mitochondria contact sites have started to emerge in the past years

88   (Gatta and Levine 2017), including the Mitochondrial Ca^{2+} Uniporter (MCU)–Voltage

89   Dependent Anion Channel (VDAC)–Glucose Regulated Protein 75 (GRP75)–Inositol

90   Triphosphate Receptor (IP3R) machinery involved in Ca^{2+} import from the ER to

91   mitochondria (Rizzuto et al. 2009), the Protein tyrosine phosphatase interacting

92   protein 51 (PTPIP51)–Vesicle-associated membrane protein-associated protein B

93   (VAPB) complex (Stoica et al 2014) alteration of which induces defects in ER-

94   mitochondria tethering and Ca^{2+} exchanges, and Pdzd8, a recently identified

95   tethering protein and proposed paralog of the ERMES subunit Mmm1, also required

96   for the regulation of ER-mitochondria contacts and mitochondrial Ca^{2+} uptake

97   (Hirabayashi, Kwon et al., 2017). However, none of these proteins has been directly

98   involved in non-vesicular lipid transport between ER and mitochondrial membranes.

99   Lately, a mammalian LTP, VPS13A, has been shown to localize at membrane

100   contact sites including those between ER and mitochondria, but its function in lipid

101   transport at these sites has not been elucidated yet (Kumar, Leonzino et al., 2018).

102   The Oxysterol binding protein (OSBP)-related proteins constitute a large family of

103   LTPs conserved from yeast (Osh) to humans (ORP) and localized to different

104   subcellular sites, shown in several cases to be membrane contact sites. A common

105   feature of all ORPs is the presence of an OSBP-related lipid-binding/transfer (ORD)

106   domain. Most ORP proteins contain a two phenylalanines (FF) in an acidic tract

107   (FFAT)-motif that binds ER-localized VAP proteins and a pleckstrin homology (PH)

108   domain that interacts with lipids or proteins in distinct non-ER organelle membranes.

109   Two members of this family, ORP5 and ORP8, do not contain an FFAT motif but are

110   directly anchored to the ER through a C-terminal trans-membrane segment. We have

111   recently shown that ORP5 and ORP8 localize to ER-mitochondria contact sites

112   where they play a key role in maintaining mitochondrial morphology and respiratory

113   function (Galmes et al. 2016). ORP5 and ORP8 have been previously shown to

114   transfer phosphatidylserine (PS) from the cortical ER to the PM, in counter-exchange

115   with the phosphoinositides Phosphatidylinositol-4-phosphate (PI4P) and

116   Phosphatidylinositol 4,5-bisphosphate (PIP_2) (Chung et al. 2015; Ghai et al, 2017).

117   Interestingly, transport of PS occurs also at ER-mitochondria contact sites. Newly

118   synthesized PS, by the ER-localized PS-Synthase 1 (PSS1), is shuttled from the ER to

119   the outer mitochondrial membrane (OMM) and from OMM to inner mitochondrial

120   membrane (IMM) where it is rapidly converted to phosphatidylethanolamine (PE) by the

121   PS-decarboxylase enzyme PISD (Vance, 1990, Vance & Tasseva, 2013). At the IMM,

122   PE plays crucial roles in maintaining mitochondrial tubular morphology and therefore in

123   mitochondrial respiratory functions (Joshi, Thompson et al., 2012, Steenbergen,

124   Nanowski et al., 2005). Regardless of extensive studies on PS transport between ER

125   and mitochondria since its first discovery more than 20 years ago (Vance, 1990), the

126   underlying mechanisms and proteins involved are still elusive.

127   Membrane contact sites exist also between the OMM and the IMM and are

128   mediated by the Mitochondrial Intermembrane space Bridging (MIB) and Mitochondrial

129   Contact sites and Cristae junction Organizing System (MICOS) complexes. The MICOS

130   complex (composed of seven proteins: Mitofilin, CHCHD3, CHCHD6, APOO, QIL1,

131   APOOL and MINOS1) is preferentially located at Cristae Junctions (CJ), tubular

132   structures that connect the IMM to the cristae, and it is necessary for CJ formation,

133   cristae morphology and mitochondria function (Harner, Korner et al., 2011, Huynen,

134   Muhlmeister et al., 2016, Ott, Dorsch et al., 2015, Wollweber, von der Malsburg et al.,

135   2017). The integral IMM protein Mitofilin is the central component of the MICOS

136   complex and carries a large domain exposed to the mitochondria intermembrane

137   space (IMS) that interacts with the OMM Sorting and Assembly Machinery (SAM) to

138   form the MIB complex (Friedman, Mourier et al., 2015, Guarani, McNeill et al., 2015).

139   The SAM complex is constituted of SAM50 (a pore-forming β-barrel protein),

140   Metaxin1 and 2, and is involved in the membrane insertion and assembly of

141   mitochondrial β-barrel proteins, such as VDAC (Hohr, Lindau et al., 2018, Kozjak,

142   Wiedemann et al., 2003, Kozjak-Pavlovic, Ross et al., 2007) (see cartoon in Figure

143   10). However, whether and how OMM-IMM contact sites are linked to ER-

144   mitochondria contacts in mammalian cells is still largely unknown.

145   Here we show that ORP5 and ORP8 are the LTPs that transfer PS from the ER

146   to the mitochondria at ER-mitochondria contact sites in mammalian cells. We also

147   show that ORP5/8 are physically and functionally connected with Sorting Assembly

148   Machinery 50 (SAM50) and Mitofilin with which they cooperate to facilitate PS

149   transport from the ER to the mitochondrial membranes and consequently the

6

150   synthesis of mitochondrial PE. Finally, we uncover an additional role for ORP5, but not

151   ORP8, in regulating Ca^{2+} import to mitochondria, through regulation of SAM50-VDAC

152   protein levels. Our findings reveal a novel link between lipid and Ca^{2+} transport at ER-

153   mitochondria contact sites and provide mechanistic insight to the specific role of

154   ORP5 in modulating cellular senescence.

155

156   **RESULTS**

157   **ORP5 and ORP8 transport PS from the ER to the mitochondria at ER-**

158   **mitochondria contact sites**

159   We have recently reported that ORP5 and ORP8, shown to transfer lipids at ER-PM

160   contacts, localize also to ER-mitochondria contact sites (Galmes, Houcine et al., 2016).

161   However, their role in lipid transport at ER-mitochondria contacts still remains to be

162   established. Taking into account their role in counter-exchanging PS with the PM

163   phosphoinositides PI4P and PIP_2 at ER-PM contacts (Chung et al. 2015; Ghai et al,

164   2017), we hypothesized that ORP5 and ORP8 could also mediate PS transport at ER-

165   mitochondria contact sites.

166   The ORD domain of ORP8 has been shown to transfer PS (in counter-transport with

167   PI4P or PIP_2) between liposome membranes *in vitro* (Chung et al. 2015; Ghai et al,

168   2017). Since PI4P and PIP_2 are not present in mitochondrial membranes it is possible

169   that at ER-mitochondria contact sites ORP5/8 might transport other phospholipids,

170   such as PE, back to the ER. However, no study so far has ever addressed the ability

171   of ORP5 and ORP8 ORD domains (ORD5, ORD8) to transfer other phospholipids

172   between liposomes *in vitro*. First, to compare and study the role of ORD5 and ORD8

173   in the transfer of phospholipids *in vitro*, we purified the recombinant ORD5 (aa 265-

174   703) and ORD8 (aa 328-767) in bacteria (Escherichia coli) (Fig. S1a) and analyzed

175   their lipid transfer ability by measuring the transport of fluorescent phospholipids

176   (TopFluor-PS, -PC or -PE) from donor to acceptor liposomes *in vitro*. Donor

177   liposomes containing fluorescent phospholipids and biotinylated lipids (liposomes

178   composed of 1 mol% TopFluor-PS, -PC or -PE, 2 mol% of biotinylated-PE, and 97

179   mol% POPC) were first immobilized on streptavidin beads and then mixed with

180   acceptor liposomes (composed of 100 mol % POPC) in the presence or absence of

181   ORP5/8 ORD domains (Fig. 1a). After 1 hour at 37°C, acceptor liposomes were

182   recovered from the supernatant and their fluorescence was measured (Fig. 1a). Our

183   results show that both ORD5 and ORD8 transfer PS, but not PC and PE, from donor

184   to acceptor liposomes (Fig. 1b). They also reveal that ORD5 and ORD8 share

185   equivalent abilities to transfer PS *in vitro*. To confirm that fluorescent lipids were

186   indeed transferred to the acceptor liposomes, a fraction of the reaction supernatant

187   was floated on a Nycodenz density gradient by ultracentrifugation and the

188   fluorescence in the top fraction of the gradient (containing floated acceptor

189   liposomes) was measured (Figure S1b). Fluorescence of TopFluor-PS in the

190   acceptor liposomes was maintained after their floatation, confirming its effective

191   transfer between liposomes *in vitro*.

192   Next, we addressed whether ORP5 and ORP8 could mediate non-vesicular

193   transfer of PS at ER-mitochondria contact sites *in situ*. As the ER-derived PS is the

194   major precursor for mitochondrial PE, if ORP5 and ORP8 mediate non-vesicular

195   transport of PS from the ER to the mitochondria, then their absence should lead to a

196   reduction of mitochondrial PE. To test this, we used Percoll gradient-based

197   subcellular fractionation (Galmes et al. 2016) to isolate pure mitochondria from HeLa

198   cells where ORP5 or ORP8 were transiently silenced by RNAi. We chose to use a

199   transient knockdown as it overcomes the limits and/or compensatory effects on lipid

8

200   transport/biosynthetic pathways that other stable approaches could induce. The

201   purity of mitochondria and of the other subcellular fractions was verified in control,

202   ORP5 and ORP8 knockdown conditions by western blotting (WB) (Fig. 1c). As

203   controls for the purity of subcellular fractions, the samples were probed for

204   cytochrome c as mitochondrial marker and IP3R-3 as a MAM-enriched marker. All

205   markers were highly enriched in their respective fractions and were absent in the

206   others. In accord with our previous study (Galmes et al., 2016), ORP5 and ORP8

207   were enriched in the MAM fraction and absent in the mitochondria fraction of control

208   cells. On the contrary, they were strongly suppressed in ORP5 and ORP8

209   knockdown cell lysates and in the respective MAM fractions (Fig. 1c). The PE content

210   of purified mitochondria from ORP5 and ORP8 knockdown was then analyzed by

211   mass spectrometry (MS)-based lipidomics, revealing a reduction of PE levels in

212   mitochondria isolated from ORP5 and ORP8 knockdown cells of 34% and 20%,

213   respectively, as compared to control cells (Fig. 1d). Interestingly, PE levels of the

214   total cells were unchanged, indicating a specific effect of ORP5 or ORP8 depletion

215   on mitochondrial PE.

216   In subsequent experiments, we measured the levels of mitochondrial PE newly

217   synthesized from the ER-derived PS by using a radiometric PS-to-PE conversion

218   assay *in situ* (Shiao, Lupo et al., 1995) in silenced or control HeLa cells (Fig. 1e).

219   This assay allows the monitoring of PS transfer from the ER to mitochondria by

220   measuring the levels of radioactive PS and PS-derived PE by thin layer

221   chromatography (TLC) after 18h of incorporation of radioactive L-[^{3}H(G)]-serine into

222   the cells. A significant decrease in the levels of newly synthetized PE was found in

223   ORP5 knockdown and in ORP5+ORP8 double-knockdown cells (Fig. 1e). The

224   decrease was stronger in ORP5+ORP8 double-knockdown cells, indicating a

225 cooperative effect of ORP5 and ORP8 in this process. A slight decrease was also

226 found in ORP8 knockdown cells, although not statistically significant, suggesting a

227 major role of ORP5 compared to ORP8 in PS transfer at ER-mitochondria contact

228 sites *in situ*. As [^{3}H]-serine radioactivity could be incorporated to PE also via an

229 alternative pathway involving sphingosine (Hanada, Nishijima et al., 1992), we next

230 sought to address the contribution of this pathway to PE labeling, by repeating the

231 experiments in control and ORP5 knockdown cells in the presence of β-chloro-L-

232 alanine, an inhibitor of serine palmitoyltransferase (Chen, Born et al., 1993). The PS-

233 to-PE conversion was not significantly affected in both control (~3% of reduction) and

234 ORP5 knockdown cells (~9% of reduction). On the contrary, PS-to-PE conversion

235 was significantly reduced in treated and untreated ORP5 knockdown cells (~17% and

236 ~23% respectively), as compared to control (Fig. 1f). These data show that more

237 than 90% of serine labeling occurs via PS in HeLa cells, that is in accord with a

238 previous work in another cell type, the BHK cells, showing that only a minor PE

239 species are labeled from the sphingosine-PE pathway (Heikinheimo & Somerharju,

240 1998). Lastly, the decrease in PE could be simply due to a decrease in the protein

241 levels of PS-decarboxylase (PISD) or in the PS-Synthase 1 (PSS1) enzymes

242 mediating PS-to-PE conversion on mitochondria or PS synthesis in the ER,

243 respectively. To exclude this possibility we analyzed the protein levels of PISD and

244 PSS1 enzymes by WB in ORP5, ORP8, ORP5+ORP8 knockdown cells and

245 compared them to control cells (Fig. 1g). We found no significant difference but

246 rather a slight increase in upon ORP5 and/or ORP8 knockdowns. Overall these data

247 confirm that the reduction in mitochondrial PE induced by depletion of ORP5 is

248 essentially due to the decrease in PS transfer from the ER to the mitochondria (Fig.

249 1h).

250

ORP5 and ORP8 knockdown affect mitochondria morphology and respiratory function but not the abundance of ER-mitochondria contact sites

Even a modest reduction (22-27%) of mitochondrial PE levels in mammalian cells have been shown to profoundly alter the morphology of mitochondrial cristae as well as mitochondria functions (Tasseva, Bai et al., 2013). Thus, the decrease in mitochondrial PE in ORP5 and ORP8 knockdowns is in accord with our previous electron microscopy (EM) observations that knockdown of ORP5 or ORP8 alters the architecture of the cristae, while ER-mitochondria contact sites with normal morphology were still visible (Galmes et al., 2016). However, our previous study did not rule out that these contact sites could be affected in their number/size. To test whether the effects on PS transport at ER-mitochondria contacts were specific of ORP5 and ORP8 loss of function or simply due to a decrease of ER-mitochondria contacts induced by their knockdown, we quantified the abundance of ER-mitochondria contact sites by EM in control and ORP5, ORP8, ORP5+ORP8 knockdown cells. To facilitate the visualization of the ER we transfected the cells with a HRP-KDEL construct (carrying a horseradish peroxidase (HRP) tagged with an ER retention motif) that stains the ER with a dark signal. Our quantifications revealed that ORP5, ORP8 or ORP5+ORP8 knockdowns did not affect the extent of ER-mitochondria contact sites (Fig. 2a-2b). These results indicate that ORP5 and ORP8 act exclusively as LTPs and not as tethers (Fig. 1h). Additionally, 52% of mitochondria in ORP5+ORP8 double-knockdown cells display aberrant cristae morphology versus 9% in control cells (Fig. 2a-2c). These defects in cristae morphology were similar to those previously shown in the case of ORP5 and ORP8 individual knockdowns (Galmes et al., 2016). However, the % of mitochondria with altered morphology in ORP5+ORP8 double-knockdown cells was higher as

276   compared to ORP8 knockdown (Galmes et al., 2016), possibly reflecting the stronger

277   effect of ORP5+ORP8 double-knockdown on PS transport at ER-mitochondria

278   contact sites. We had previously shown that ORP5 knockdown induced a reduction

279   in the basal mitochondrial oxygen consumption rate (OCR_{BAS}), indicative of reduced

280   mitochondria respiratory activity (Galmes et al., 2016). However, it remained still

281   questioned whether ORP8 could partially compensate the reduced OCR_{BAS} and/or if

282   this reduction could be exacerbated under metabolic stress conditions. Thus, we

283   monitored mitochondria OCR in control, in ORP5 and in ORP5+ORP8 double-

284   knockdown cells in basal and in stress conditions (Fig. 2d). ORP5 knockdown induced a

285   significant reduction in both OCR_{BAS} (~37%) and OCR upon FCCP treatment (OCR_{FCCP}) (~36%).

286   Interestingly, the decrease in in OCR_{BAS} and OCR_{FCCP} measured upon ORP5+ORP8

287   double-knockdown was quite similar to the decrease in ORP5 knockdown. These

288   data uncover a major role of ORP5 in preserving mitochondrial respiratory activity, in

289   accord with its major role in PS transfer at ER-mitochondria contact sites.

290

291   **ER-mitochondria contact sites marked by ORP5/8 are physically connected to**

292   **mitochondrial membranes via ORP5/8 interaction with the mitochondrial**

293   **intermembrane space bridging (MIB) complex**

294   To investigate whether ORP5/8 localize to specific ER-mitochondria contact site

295   subdomains we performed a morphological analysis of ORP5 localization by

296   immuno-EM (IEM) on ultrathin cryosections from HeLa cells transfected with HA-

297   ORP5 or EGFP-ORP5. The advantage of analyzing ORP5 localization is its

298   preferential localization to contact sites as compared to ORP8 (Galmes et al. 2016),

299   which remains also largely present within the reticular ER. Interestingly, the majority

300   of ORP5 gold particles was found to localize to ER elements in a very close proximity

301   (86% within 0-100 nm distances, 50% of which within 50 nm) to the CJ (arrow, Fig.

302   2a-b), tubular structures that connect the IMM to the cristae. To exclude that ORP5

303   localization near CJ is not a consequence of its distribution throughout the ER

304   membranes, we sought to determine if other ER proteins have a similar frequency of

305   proximity to CJ. Thus we compared ORP5 localization to Sec61β, a subunit of the

306   Sec61 complex involved in protein translocation in the ER, that is present in ER

307   elements distributed throughout the cells and very little at ER-mitochondria contact

308   sites (Galmes et al. 2016). Co-immunolabeling of EGFP-ORP5 or EGFP-Sec61β and

309   protein disulfide isomerase (PDI) to stain the ER, confirmed ORP5 localization in ER

310   elements close to CJ (arrow, Fig. 3c) but not of Sec61β, the bulk of which localized

311   on ER membranes distant from the CJ (0% within 0-100nm and 69% >200nm

312   distance) even when close to mitochondria (Fig. 3b and arrowheads in Fig. 3c).

313   Hence, our results support the conclusion that ORP5 specifically localizes to ER-

314   mitochondria contact sites closely associated to CJ. Interestingly, in yeast, CJ were

315   shown to be closely associated to OMM-IMM contact sites tethered by the MICOS

316   complex (Harner et al., 2011). IEM analysis using Mitofilin-EGFP, an EGFP-tagged

317   construct of the human orthologue of the central component of the MICOS complex,

318   confirmed that human Mitofilin, similarly to its yeast orthologue, preferentially

319   localizes to the IMM in close proximity of CJ and in the cristae that arise from them

320   (arrow, Fig. 3a). These results suggest that ER-mitochondria contact sites where

321   ORP5 localizes could be physically connected to the intra-mitochondrial membrane

322   contact sites near CJ.

323   To identify specific binding partners of ORP5 at ER-mitochondria contact sites

324   we carried out a MS-analysis on GFP-pull downs from cells expressing EGFP-ORP5,

325   EGFP-ORP5ΔPH (an ORP5 mutant lacking the PM-targeting PH domain that is

13

326   localized at ER-mitochondria but not at ER-PM contact sites), or EGFP alone as a

327   control (Fig. 4a). As expected, the highest hit detected in both EGFP-ORP5 and

328   EGFP-ORP5ΔPH pull-downs was its binding partner ORP8, with which ORP5 forms

329   a complex at contact sites including MAMs (Chung, Torta et al., 2015, Galmes et al.,

330   2016). Other major hits comprise several outer mitochondrial membrane proteins

331   (listed in Fig. 4a), including the mitochondrial outer membrane protein PTPIP51, a

332   previously reported interacting partner of ORP5 (Galmes et al., 2016).

333   Interestingly, among these proteins the Sorting Assembly Machinery Subunit 50

334   (SAM50), a central component of the SAM protein complex involved in the import

335   and assembly of mitochondria β-barrel proteins in the OMM (Hohr et al., 2018), had

336   one of the highest scores. SAM50 is part of the Mitochondrial intermembrane space

337   bridging (MIB) complex, composed of metaxin-1, metaxin-2 and the MICOS complex

338   that anchors the OMM to the IMM at CJ (Huynen et al., 2016, Ott et al., 2015).

339   SAM50 is also known to directly bind the central component of the MICOS complex

340   Mitofilin (Ott et al., 2015). Consistently, Mitofilin was also detected in the MS of

341   EGFP-ORP5 and EGFP-ORP5ΔPH pull-downs (Fig. 4a). Interestingly, SAM50 and

342   Mitofilin showed a higher interaction score in EGFP-ORP5ΔPH immunoprecipitates,

343   as compared to EGFP-ORP5. Of note, metaxin-2, another component of the MIB

344   complex, localized to the outer mitochondrial membrane, was also detected in the

345   MS of immunoprecipitated EGFP-ORP5ΔPH, whereas its score in the EGFP-ORP5

346   was lower than the assigned threshold (50) (Fig. 4a). To verify that the

347   overexpression of ORP5 or ORP5ΔPH did not affect the protein levels of SAM50 and

348   Mitofilin, WB analysis using anti-actin as loading control was carried out on cells

349   expressing EGFP-ORP5, EGFP-ORP5ΔPH or EGFP alone. Our results show that

350   neither EGFP-ORP5 nor EGFP-ORP5ΔPH overexpression alters the amount of

14

351   SAM50 and Mitofilin proteins as compared to the overexpression of EGFP alone (Fig.

352   S2b).

353   To confirm ORP5/8 interaction with SAM50 and Mitofilin, GFP-pull down

354   experiments from HeLa cells expressing EGFP-ORP5, EGFP-ORP8 or EGFP alone

355   were carried out (Fig. 4b). Consistent with the MS data, endogenous SAM50 and

356   Mitofilin were recovered with both EGFP-ORP5 and EGFP-ORP8 but not with EGFP

357   alone, confirming specific interaction of ORP5 and ORP8 with SAM50 and Mitofilin.

358   Of interest, the interaction of SAM50 and Mitofilin with EGFP-ORP5 was stronger

359   than with EGFP-ORP8. To visualize the sites of this interaction we performed

360   confocal imaging of HeLa cells transfected with EGFP-ORP5 and stained with anti-

361   Mitofilin antibody, as Mitofilin is the major component of the MICOS complex. We

362   observed strong co-localization of non-cortical ORP5-labeled ER elements (MAMs)

363   and Mitofilin-enriched microdomains on mitochondria (Fig. 4c and S2a), further

364   confirming the physical association of ORP5 and the MIB/MICOS complex at ER-

365   mitochondria contact sites.

366   Next, to determine the domains involved in the interaction of ORP5 with the

367   MIB/MICOS complex GFP-pull down experiments were carried out from cells

368   expressing EGFP-tagged ORP5 (EGFP-ORP5ΔPH) or ORP8 (EGFP-ORP8ΔPH) PH

369   domain deleted constructs, and compared to the full-length proteins (EGFP-ORP5

370   and EGFP-ORP8) or to the EGFP alone. In accord with the MS data, the deletion of

371   the PH domain increased ORP5 interaction with SAM50, as compared to the full-

372   length protein (Fig. 4d). In addition, EGFP-ORP8ΔPH interaction with SAM50 was

373   higher than of EGFP-ORP8, although still lower than the interaction of EGFP-

374   ORP5ΔPH or even EGFP-ORP5 with SAM50.

375   As the PH domain is not required for the interaction with SAM50 we further

376   investigated the role of the other domains of ORP5 in such interaction by

377   immunoprecipitating ORP5 deletion mutants for the ORD and the transmembrane

378   (TM) domains (EGFP-ORP5ΔORD, EGFP-ORP5ΔTM). While the deletion of the

379   ORD domain did not affect the interaction between ORP5 and SAM50, the deletion of

380   the TM domain decreased the amount of SAM50 co-immunoprecipitated with ORP5,

381   indicating that ORP5 should be properly anchored to the ER to localize at ER-

382   mitochondria contact sites and to interact with SAM50 (Fig. 4d).

383   To observe ORP5 and SAM50 localization we performed confocal analysis on

384   cells expressing EGFP-ORP5 or EGFP-ORP5ΔPH and stained with an anti-SAM50

385   antibody to look at the endogenous protein (Fig. 4e). As expected, endogenous

386   SAM50 localizes on mitochondria in cells stained with Mitotracker and, as previously

387   shown (Galmes et al., 2016), EGFP-ORP5 localizes to both ER-PM and ER-

388   mitochondria contact sites while the EGFP-ORP5ΔPH loses its localization to ER-PM

389   contacts. Both full-length and ΔPH constructs co-localized with endogenous SAM50

390   at ER elements in contact with mitochondria (Fig. 4e). However, this was more

391   evident in the case of EGFP-ORP5ΔPH (bottom image, Fig. 4e).

392   Since ORP5 is not detectable at endogenous levels by microscopy, to assess

393   ORP5 and SAM50 localization when both proteins are expressed at similar levels, we

394   generated a C-terminally tagged construct of SAM50 (SAM50-HA) and co-expressed

395   this construct with EGFP-tagged full-length ORP5 or ORP8 and ΔPH mutant

396   constructs. First, we verified that SAM50-HA was properly localized to mitochondria

397   by confocal microscopy (Fig. S2c). Then we co-expressed SAM50-HA together with

398   EGFP-ORP5, EGFP-ORP5ΔPH or EGFP-ORP5is2 (a natural variant of ORP5

399   deleted of most of its PH domain, K134-V201) (Fig. S2d, S2e, S2f) and in parallel

400   experiments with EGFP-ORP8 or EGFP-ORP8ΔPH (Fig. S3a, S3b) in HeLa cells

401   and analyzed their localization by confocal microscopy. ORP5-containing ER

402   elements were found in close proximity to SAM50-stained mitochondria. This effect

403   was more prominent in the case of EGFP-ORP5ΔPH or EGFP-ORP5is2 (Fig S2e,

404   S2f), but less evident in the case of EGFP-ORP8 or EGFP-ORP8ΔPH (Fig. S3a,

405   S3b), consistent with the stronger interaction of ORP5 with SAM50 as compared to

406   ORP8. However, we did not observe a shift in the localization of ORP5 from the

407   cortical ER (in the case of full-length ORP5/8) or from the reticular ER (in the case of

408   ORP5/8 ΔPH) to the non-cortical ER in close proximity to mitochondria, as previously

409   shown for both ORP5 and ORP8 when co-expressed with PTPIP51 (Galmes et al

410   2016). This might be explained by the fact that, while PTPIP51 is a tethering protein

411   that expands ER-mitochondria contact sites when overexpressed, SAM50 does not

412   function as an ER-mitochondria tether.

413   To test whether the interaction of ORP5 with the MIB complex could facilitate

414   the non-vesicular transfer of PS from the ER to the mitochondrial membranes (and

415   consequently synthesis of mitochondrial PE) we depleted ORP5, SAM50 or

416   Mitofilin alone or in combination by RNAi and analyzed the content in

417   mitochondrial PE newly synthesized from PS using the same radiometric PS-to-

418   PE conversion assay *in situ* described above. Robust knockdown of ORP5,

419   SAM50 or Mitofilin was confirmed by western blotting after 48 hours (Fig. 5a).

420   Analysis of PS-derived newly synthetized PE revealed a significant decrease in

421   PE in ORP5 (Fig. 1d and Fig. 3b) and Mitofilin knockdown cells (Fig. 5b).

422   Moreover, the double-knockdown of ORP5 and Mitofilin had an additive effect,

423   supporting a cooperation of these two proteins in the same process (PS

424   transport/PE synthesis). However, the levels of PE were not changed in SAM50

17

425 knockdown cells as compared to control. This can be explained by the fact that

426 other subunits of the MIB complex (i.e. Mitofilin) might compensate for its

427 depletion. Indeed, levels of Mitofilin are increased in SAM50 knockdown cells (Fig.

428 5a). Accordingly, the double-silencing of SAM50 and either ORP5 or Mitofilin had

429 a significant impact on PE synthesis (Fig. 5b). Moreover, the reduction in PE was

430 even stronger as compared to the individual knockdowns indicating that disruption

431 of both a component implicated in a direct transport of PS at ER-mitochondria

432 contact sites and a component of the OMM-IMM tethering complex has a

433 significant impact on PE synthesis.

434 To verify the possibility of an indirect effect of Mitofilin or SAM50 silencing on the

435 morphology and abundance of ER-mitochondria contacts we carried out a

436 morphological analysis by conventional EM in all these knockdown conditions and

437 quantified ER-mitochondria contacts by HRP-KDEL EM (to stain the ER) in Mitofilin

438 or SAM50 silenced cells. Morphological analysis by conventional EM showed that

439 transient (48 hours) knockdowns of SAM50 and Mitofilin, as well as double-

440 knockdowns of ORP5+Mitofilin, ORP5+SAM50 and SAM50+Mitofilin, induce

441 formation of multilamellar cristae, almost devoid of CJ (Fig. S4a-b), complementing

442 previous observations obtained by other groups through stable disruption of the

443 MICOS/MIB functions (Ding, Wu et al., 2015, Ott et al., 2015). However, in all

444 knockdown conditions analyzed ER-mitochondria contact sites were still present and

445 their morphology not altered. Quantitative morphological analysis by HRP-KDEL EM

446 in control and Mitofilin or SAM50 silenced cells confirmed that the abundance of ER-

447 mitochondria contact sites was not altered by Mitofilin or SAM50 knockdown (Fig. 5c-

448 d) indicating that the effects on PS-derived PE synthesis were specifically due to

449 Mitofilin or SAM50 loss of function effects on intra-mitochondrial membrane bridges.

450   Overall our results indicate that ER-mitochondria contacts where ORP5/8 localize

451   are physically linked to intra-mitochondria contacts where the components of the

452   MIB/MICOS complex reside, and this association facilitates the transfer of PS from

453   the OMM to the IMM for synthesis of PE.

454

455   **ORP5 additionally regulates VDAC-mediated Ca^{2+} import to mitochondria by**

456   **acting on the MIB component SAM50**

457   To get further insights into the functional link between ORP5/8 and the

458   MIB/MICOS complex we explored whether ORP5 and ORP8 knockdowns might

459   affect the expression and/or the localization of SAM50 and Mitofilin. Interestingly

460   when we analyzed cell lysates by WB, we found that SAM50 and Mitofilin protein

461   expression was significantly and specifically increased in ORP5- but not in ORP8

462   knockdown cells, as compared to control cells (Fig. 6a-b). The effects of ORP5

463   silencing were specific for SAM50 and Mitofilin, as other mitochondrial proteins

464   (Cytochrome c, CV-ATP5A) or proteins of the general ER (PDI) and of the MAMs

465   (VAPB) were not affected (Fig. S5a). This could also be observed by IF analysis

466   where the increase in SAM50 staining on mitochondria is specific to ORP5

467   knockdown (Fig. 6c, S5b-c).

468   Intriguingly, such increase in SAM50 was accompanied by a dramatic

469   accumulation in the voltage-dependent anion channel VDAC, a 19-stranded

470   transmembrane β-barrel protein (Colombini, 2012) that requires SAM50 for its

471   biogenesis and insertion in the OMM (Hohr et al., 2018). These results suggest that the

472   accumulation of VDAC protein in ORP5 knockdown cells is due to the parallel

473   increase of SAM50. Indeed, overexpression of SAM50-HA in control HeLa cells was

474   sufficient to induce an increase in endogenous VDAC (Fig. S5d). Also, the

19

475　simultaneous knockdowns of ORP5 and SAM50 rescued the increase in VDAC,

476　confirming that its accumulation in ORP5 knockdown cells was due to the

477　accumulation of SAM50. Interestingly, ORP5 and SAM50 double-knockdown did not

478　rescue the increased protein levels of Mitofilin (Fig. 6a-b), in accord with the fact that

479　SAM50 knockdown alone also increased the protein levels of Mitofilin. To verify that

480　the increase in their protein amounts did not depend on the increase in their

481　transcripts we quantified the transcript levels of ORP5, SAM50 and the three VDAC

482　isoforms (VDAC1, 2 and 3) by real-time PCR upon ORP5 or SAM50 knockdown (Fig.

483　6d, S5e). The quantity of SAM50 and Mitofilin transcripts was unaffected by ORP5

484　silencing, and VDAC1 transcript levels were even slightly reduced, possibly reflecting

485　a compensatory mechanism induced by the increase in VDAC protein. Similarly,

486　VDAC and Mitofilin transcript levels were not affected in the absence of SAM50,

487　although transcript levels of ORP5 were increased, possibly reflecting a regulatory

488　mechanism controlled by the levels of SAM50. Overall, these data indicate that

489　ORP5 knockdown induces an accumulation of SAM50 and VDAC (SAM50-

490　dependent) proteins in the absence of major effects on the corresponding mRNAs.

491　　　To confirm that the accumulation of SAM50-VDAC was indeed due to ORP5

492　function at ER-mitochondria contact sites and not from indirect effects of ORP5 at

493　ER-PM contacts we re-expressed EGFP-ORP5is2 (a ORP5 isoform lacking the PH

494　domain and thus localized at MAMs but not at ER-PM contacts) in Ctrl and ORP5

495　knockdown cells and analyzed the protein levels of SAM50 and VDAC by WB (Fig.

496　6e). As a control EGFP alone was transfected. A complete rescue of SAM50 and

497　VDAC levels was observed in ORP5 knockdown cells transfected with EGFP-

498　ORP5is2 but not in cells transfected with the EGFP alone. These results confirmed

20

499 that the increase in SAM50 and VDAC was the effect of the specific loss of function

500 of ORP5 at MAMs.

501 Given the role of ORP5 in regulating levels of mitochondrial PE, it is possible that

502 the increase in SAM50, and consequently of VDAC, observed in ORP5 knockdown

503 cells is linked to the decrease in PE on mitochondria membranes. Thus, we

504 investigated if reducing the levels of mitochondrial PE by knocking down the PS-

505 decarboxylase PISD, enzyme that converts PS in PE in mitochondria, induces a

506 similar increase in SAM50-VDAC proteins (Fig. 6f). WB analysis confirmed robust

507 suppression of PISD and an increase in SAM50 and VDAC, similarly to that observed

508 upon ORP5 knockdown. These data strongly suggest that the decrease of PE in

509 ORP5 depleted cells is responsible for the abnormal stabilization of SAM50 and

510 VDAC in mitochondrial membranes. They also strengthen the importance of having

511 proper levels of PE to ensure correct turnover and function of mitochondrial protein

512 complexes.

513 As VDAC is one of the major mitochondrial players in mediating Ca^{2+} transport

514 and signaling between ER and mitochondria (Rapizzi, Pinton et al., 2002), we next

515 investigated if ORP5 knockdown could regulate Ca^{2+} influx from the ER to

516 mitochondria in living cells. We first used a ratiometric Ca^{2+} indicator selectively

517 targeted to mitochondria (mt-Pericam) which is based on a circularly permuted yellow

518 fluorescent protein fused to calmodulin (Nagai, Sawano et al., 2001). Upon binding to

519 Ca^{2+}, the excitation peak of mt-Pericam shifts from 415 nm to 494 nm while the

520 emission spectrum remains unchanged around 515 nm, allowing us to quantify rapid

521 changes in mitochondrial Ca^{2+}. We thus transfected ORP5, ORP8 or Ctrl siRNA-

522 treated cells with mt-Pericam and then measured mitochondrial Ca^{2+} fluxes, in

523 response to histamine, by live-cell spinning disk microscopy (Fig. 7a-b). Soon after

524 the addition of histamine, mt-Pericam fluorescence ratio (488/405) rapidly increased

525 in all conditions, reflecting the increase in mitochondrial Ca^{2+} influx triggered by the

526 histamine treatment. However, interestingly, ORP5 knockdown cells showed a

527 significantly higher increase as compared to ORP8 knockdown and to control cells.

528 Quantification of the maximum amplitude of the response after histamine treatment

529 (expressed as R_{max}/R_0, where R is the 488/405 ratio, R_{max} is the maximum

530 fluorescence ratio after histamine addition and R_0 the basal ratio before histamine

531 addition) confirmed that ORP5 but not ORP8 silencing induced a statistically relevant

532 increase of mitochondrial Ca^{2+} influx, triggered by the addition of histamine, as

533 compared to control cells (Fig. 7b).

534   Passive entry of Ca^{2+} into mitochondria can be driven by large negative

535 membrane potential of mitochondria and occurs through the mitochondrial Ca^{2+}

536 uniporter MCU spanning the IMM (Patron, Raffaello et al., 2013). To be sure that the

537 increase of mitochondrial Ca^{2+} upon ORP5 knockdown was not indirectly due to a

538 change of mitochondrial membrane potential, we performed flow cytometric analysis

539 in ORP5 or ORP8 knockdown cells. Knockdown cells were loaded with the

540 mitochondrial membrane potential sensitive dye TMRE (Tetramethylrhodamine ethyl

541 ester), in the presence (or absence) of the mitochondrial oxidative phosphorylation

542 uncoupler CCCP (Carbonyl cyanide 3-chlorophenylhydrazone) to induce membrane

543 depolarization (Fig. S6a). Neither ORP5 nor ORP8 knockdown altered mitochondrial

544 membrane potential as compared to control cells, even in presence of CCCP that

545 strongly decreases TMRE fluorescence intensity (Fig. S6a), showing that the effect of

546 ORP5 knockdown on Ca^{2+} is not due to a change of mitochondrial membrane

547 potential.

22

548   To further study the role of ORP5 in the regulation of Ca^{2+} homeostasis a parallel

549   set of experiments was performed using another type of Ca^{2+}-probe, the red

550   fluorescent genetically encoded Ca^{2+} indicator (R-GECO) and its two variants

551   selectively-targeted to mitochondria (mito-LAR-GECO) or ER (ER-LAR-GECO) to

552   respectively measure cytosolic, mitochondrial and ER Ca^{2+} in living cells (Fig. 7c-e).

553   These experiments confirmed that ORP5 silencing increases mitochondrial Ca^{2+}

554   uptake (Fig. 7c). The increase in mitochondrial Ca^{2+} uptake triggered by histamine

555   treatment was accompanied by a decrease in ER Ca^{2+} and an increase in cytosolic

556   Ca^{2+} in all conditions (Fig. 7d-e). Interestingly, no statistically relevant differences of

557   the decrease ER Ca^{2+} were measured between ORP5 silenced and control cells.

558   This indicates that the effects on mitochondrial Ca^{2+} fluxes observed in ORP5 do not

559   depend on the modification of ER Ca^{2+} storage or release. An increase in cytosolic Ca^{2+}

560   was measured in ORP5 and ORP8 silenced cells as compared to control. As this

561   increase was not specific for ORP5 silencing, it likely reflects a common role of

562   ORP5/8 in Ca^{2+} homeostasis at ER-PM contact sites, as recently proposed (Pulli,

563   Lassila et al., 2018).

564   So far, our data show that the absence of ORP5 increases mitochondrial Ca^{2+}

565   possibly by acting on the mitochondrial proteins SAM50 and VDAC, supported by the

566   specific accumulation of these two proteins in the absence of ORP5. To confirm that

567   the increase of mitochondrial Ca^{2+} in ORP5-silenced cells was indeed dependent on

568   VDAC and SAM50, we measured mitochondrial Ca^{2+} using mt-Pericam in VDAC- (all

569   three isoforms), ORP5+VDAC- and ORP5+SAM50- doubly-silenced cells. A

570   significant decrease in VDAC and SAM50 as well as ORP5 levels was detected by

571   WB in the corresponding silenced cells (Fig. 8a and Fig. 6a). Even though the

572   increased level of VDAC protein induced by the absence of ORP5 was not

23

573   completely rescued in ORP5+VDAC or ORP5+SAM50 knockdowns, the increase in

574   mitochondrial Ca^{2+} phenotype was significantly rescued to control levels and partially

575   rescued in ORP5+VDAC and ORP5+SAM50-silenced cells, respectively (Fig. 8b and

576   c). Overall, these results demonstrated that ORP5 plays an additional role in

577   regulating import of mitochondrial Ca^{2+} through regulation of SAM50 and VDAC

578   proteins.

579

580   **ORP5 knockdown induces cell senescence in a SAM50-dependent manner**

581   Accumulation of mitochondrial Ca^{2+} has been shown to be involved in both

582   apoptotic cell death and senescence (permanent cell proliferation arrest) (Wiel,

583   Lallet-Daher et al., 2014). Interestingly, it has also been shown that ORP5 expression

584   promotes cell proliferation (Du, Zadoorian et al., 2018). As our data show a new role

585   of ORP5 in regulating Ca^{2+} import to mitochondria at ER-mitochondria contact sites

586   (Fig. 8), we were wondering if ORP5 could mediate cellular processes such as

587   apoptosis and senescence. To address this question, we decided to study both

588   apoptosis and senescence in ORP5 depleted cells.

589   For apoptosis, we performed immunofluorescence and stained with anti-cleaved

590   caspase-3 (to detect apoptotic cells) HeLa cells transfected with control siRNA or

591   siRNA against ORP5 or ORP8. We also treated the knockdown cells with

592   staurosporine to induce apoptosis or with DMSO as vehicle control (Fig. S4b).

593   Quantification of the percentage of cleaved caspase-3 positive cells (% of total cells)

594   in all conditions showed no significant difference between ORPs knockdown and

595   control cells (Fig. S6b), even in presence of staurosporine, showing that in these

596   conditions transient silencing of ORP5/8 does not induce apoptosis.

24

597   To study cellular senescence we performed knockdown of ORP5 in MRC5

598   normal human fibroblasts that are a good model for senescence studies (Ma,

599   Warnier et al., 2018). We first looked at cell proliferation using crystal violet staining

600   in both control and ORP5 knockdown cells (Fig. 9a). A significant decrease of the cell

601   number was detected in ORP5 depleted cells compared to control (Fig. 9a). This

602   decrease of the cell number in ORP5 knockdown cells could be correlated with an

603   increase of the Senescence-associated β –galactosidase (SA β-gal) staining as

604   compared to control (Fig. 9a). Accordingly, these results were corroborated by qRT-

605   PCR analysis showing a significant increase of the senescence markers p16 and p21

606   and a significant decrease of the proliferation marker Ki67 in ORP5 knockdown cells

607   compared to control (Fig. 9b). Because we have shown that ORP5 knockdown

608   induces an elevation of mitochondrial Ca^{2+} via a SAM50-dependent accumulation of

609   VDAC, we hypothesized that the induction of senescence in MRC5 cells could also

610   be due to the effect of ORP5 on SAM50. Thus, we decided to perform a double-

611   knockdown of ORP5 and SAM50 in MCR5 cells. In accord with our hypothesis, this

612   double-silencing partially rescued the senescence phenotype found in ORP5

613   knockdown cells. ORP5+SAM50 double-knockdown cells displayed increased

614   proliferation and underwent less senescence as compared to ORP5 single

615   knockdown cells (Fig. 9c). To verify that this effect on cellular senescence was

616   specific to ORP5, given its role in mitochondria Ca^{2+} regulation, we performed in

617   parallel a knockdown of ORP8 in MRC5 cells. Differently to ORP5, ORP8 knockdown

618   did not induce cell senescence (Fig. 9c). Taken together, these data reveal a novel

619   specific role of ORP5, involving SAM50, in regulating the cellular senescence in

620   MRC5 cells.

621

622 **DISCUSSION**

623   In this study, by using a combination of *in vitro* and *in situ* biochemical and imaging

624 approaches, we describe a new function of ORP5/8 in the maintenance of mitochondrial

625 levels of PE, an essential phospholipid of mitochondria, in mammalian cells. Importantly,

626 we provide the first evidence of LTPs (ORP5 and ORP8) directly mediating non-

627 vesicular transfer of PS at ER-mitochondria contact sites, from the ER to the

628 mitochondria where it is converted into PE.

629   In yeast, large tethering complexes such as the ERMES and the ER-Membrane

630 protein Complex (EMC) have been previously involved in phospholipid trafficking (PC

631 and PS, respectively) between the ER and the mitochondrial membranes (Tamura &

632 Endo, 2017) (Lang, John Peter et al., 2015). For instance, three subunits of the

633 ERMES complex contain a Synaptotagmin-like Mitochondria lipid binding Protein

634 (SMP) domain that forms a hydrophobic lipid transport cavity shared by other

635 proteins of the tubular lipid-binding protein TULIP superfamily (Kopec, Alva et al.,

636 2010, Reinisch & De Camilli, 2016). However, a direct role (independent of its

637 tethering function) of ERMES in lipid transport at ER-mitochondria contact sites is still

638 questioned. For a long time homologues of the ERMES complex have not been

639 identified in metazoan. Hirabayashi et al. recently showed that the SMP-containing

640 protein PDZD8 is involved in ER-mitochondria tethering and in the regulation of Ca^{2+}

641 dynamics in mammalian neurons (Hirabayashi et al., 2017). Although PDZD8 is a

642 structural and functional paralogous of the Mmm1 subunit of the ERMES complex

643 (Wideman, Balacco et al., 2018), its function in lipid transport at ER-mitochondria

644 contact sites remain unclear. The EMC complex, which has been involved in PS

645 shuttling at ER-mitochondria contact sites in yeast, is instead highly conserved in

646 metazoans (Wideman, 2015). However, no lipid-binding/transfer domain has been

647 found in the EMC proteins, indicating that their implication in lipid transfer at ER-

648 mitochondria contacts is linked to their tethering function rather than to a direct lipid

649 transfer activity. Recently, the mammalian LTP VPS13A has been shown to localize

650 to contact sites including ER-mitochondria contacts (Kumar et al., 2018). VPS13A

651 contains a lipid-binding domain (VPS13α) that has the ability to harbor multiple

652 phospholipids at once and transfer them between liposomes *in vitro*. However, its

653 role in lipid transfer at membrane contact sites *in situ* has not yet been established.

654 Differently from the SMP and VPS13α that can simultaneously host multiple

655 phospholipids, the ORD domain of Osh/ORPs forms a cavity that can host only one

656 lipid at a time (Maeda, Anand et al., 2013, Wang, Ma et al., 2019).

657   ORP5 and ORP8 have recently been shown to counter-exchange PS with the PM

658 phosphoinositides PI4P and PIP_2 at ER-PM contact sites in HeLa cells (Chung et al.,

659 2015, Ghai, Du et al., 2017). However, PI4P and PIP_2 are not present on the

660 mitochondrial membranes, while PE is highly abundant in these membranes, in

661 addition to being an essential lipid of all biological membranes. Our *in vitro* data show

662 that the ORD domains of ORP5 and ORP8 transport PS, but not other phospholipids

663 such as PE and PC, indicating a specific role of ORP5/8 in PS transport and excluding

664 the possibility that ORP5/8 might also participate in the transport of a fraction of PE

665 back to the ER. It is possible that ORP5/8 cooperate with other LTPs, such as VPS13A,

666 for the exchange of other lipids (including PE) at ER-mitochondria contact sites.

667 Importantly, we have confirmed the role of ORP5/8 in PS transfer by measuring a

668 decrease of PS-derived mitochondrial PE in ORP5 depleted HeLa cells *in situ* (and

669 even more upon ORP5+8 silencing, although the effect of ORP5 depletion was

670 predominant as compared to ORP8) as well as a reduction of total PE in

671 mitochondria isolated from these cells (Fig. 1c-f). Accordingly, the knockdown of

672 ORP5/8 affects cristae morphology (Fig. 2a, 2c) and the respiratory function of

673 mitochondria (Galmes et al., 2016)(Fig. 2d), all phenotypes that are expected in the

674 case of decrease in mitochondrial PE (Joshi et al., 2012, Steenbergen et al., 2005).

675 Our data further confirm the essential role of PE in the maintenance of mitochondria

676 structure and functions, and are in accord with those of (Tasseva et al., 2013)

677 showing that even a mild decrease of mitochondrial PE can strongly alter

678 mitochondria cristae morphology and respiratory function. Our data also suggest that

679 the gradient of PS at ER-mitochondria contacts is sufficient to trigger the ORP5/8-

680 mediated unidirectional transport of PS from the MAMs, where it is highly enriched, to

681 the mitochondria membranes, where it is rapidly converted into PE and is therefore

682 present at a very low amount. Our findings have important implications in the general

683 field of LTPs, as they suggest that the same LTP can use different means to transfer

684 lipids depending on the local gradients present at the specific membrane contact

685 sites where it is localized. They also suggest a possible new function in PS transport at

686 ER-mitochondria contact sites for the yeast orthologues of ORP5/8, Osh6/7p, whose

687 localization/function at ER-mitochondria contact sites still remain to be addressed

688 (Moser von Filseck, Copic et al., 2015).

689 Another important feature of our work is the observation that ORP5 and ORP8

690 knockdowns do not affect the extent of ER-mitochondria contact sites. These data,

691 consistent with our previous observation that ORP5/8 overexpression does not alter

692 the length of ER-mitochondria contacts (Galmes et al., 2016), confirm that the main

693 function of these proteins at MAMs is lipid transfer and not membrane tethering. This

694 is a unique feature among the LTPs that have been identified so far at MAMs. For

695 instance, modulation of the protein levels of other LTPs such as ERMES in yeast, or

696 PDZD8 and VPS13A in mammals, results in an alteration of the extent of ER-

697   mitochondria contact sites (Hirabayashi et al., 2017, Kornmann, Currie et al., 2009,

698   Kumar et al., 2018). Thus, ORP5/8 represent so far a unique tool to study lipid

699   transport at ER-mitochondria contact sites, independently of membrane tethering.

700   Importantly, our study also reveals that ORP5/8 physically interact with SAM50

701   and Mitofilin, two key components of the MIB/MICOS complex that anchor the IMM to

702   the OMM at the level of CJ (Huynen et al., 2016, Ott et al., 2015, Wollweber et al.,

703   2017). The biochemical interaction between ORP5 and SAM50/Mitofilin suggests the

704   existence of a physical link between ER-mitochondria contact sites involved in lipid

705   transport and intra-mitochondria contacts. ORP5 localization by IEM at ER-mitochondria

706   contact sites near the CJ, where Mitofilin and MICOS complex also reside, confirms the

707   existence of such tripartite membrane structure. Importantly, we also show that the *de-*

708   *novo* synthesis of mitochondrial PE requires both the lipid transfer activity of ORP5 at

709   ER-mitochondria contact sites and the tethering activity of the MIB/MICOS complex at

710   intra-mitochondrial OMM-IMM contact sites (Fig. 5b). Interestingly, recent evidence in

711   yeast suggests that, in addition to the classical PE synthesis at the IMM by the IMM-

712   localized PS decarboxylase Psd1, PE can be also synthesized *in trans* on the OMM

713   (Aaltonen, Friedman et al., 2016). Thus, it is possible that this alternative pathway,

714   which requires MIB/MICOS tethering function to bring the mitochondrial

715   intermembrane domain of PISD close to the OMM for synthesis of PE, is conserved

716   also in mammalian cells. The cooperation of ORP5 with SAM50 and Mitofilin could

717   facilitate the movement of PS from the ER to the IMM across ER-mitochondria

718   contact sites for synthesis of PE at the IMM, through the classical PE synthesis

719   pathway, but also PISD function *in trans* on the OMM through this alternative

720   biosynthetic pathway. Taken together these findings provide the first evidence of a

721   physical link between ER-OMM and OMM-IMM contact sites to facilitate transport of

722   PS from the ER to the mitochondria and PE synthesis on the mitochondrial

723   membranes (Fig. 10).

724   Finally, we uncover a specific role for ORP5, but not ORP8, in regulating

725   mitochondrial Ca^{2+} uptake, via a SAM50-VDAC axis. SAM50, in addition to being part

726   of the MIB complex, is also the major subunit of the Sorting and Assembly Machinery

727   (SAM) that mediates membrane insertion and assembly of mitochondrial β-barrel

728   proteins (Hohr et al., 2018, Kozjak et al., 2003). One of the most abundant

729   mitochondria β-barrel proteins is VDAC, which forms a pore that allows the passage of

730   small metabolites and ions such as ATP and Ca^{2+} across the OMM (Colombini, 2012).

731   VDAC exists as three isoforms (VDAC1, 2 and 3) that share common channeling

732   properties. VDAC interacts with the IP3Rs located in the ER membrane via the

733   molecular chaperone GRP75 that links the two proteins together. The interaction

734   between IP3Rs and VDACs acts as a bridge to allow the transfer of Ca^{2+} from the ER to

735   the OMM, and then from the OMM to the mitochondrial matrix through the mitochondrial

736   Ca^{2+} uniporter MCU. Ca^{2+} release from the ER to mitochondria is triggered by IP_3

737   binding to IP3Rs upon histamine treatment (Rizzuto, Marchi et al., 2009). Here we show

738   that knockdown of ORP5 increases the protein levels of SAM50 and VDAC as well as

739   the levels of histamine-induced Ca^{2+} import to mitochondria. We also confirm that the

740   additional role of ORP5 in regulating SAM50-VDAC levels is not indirectly due to ORP5

741   function at ER-PM contacts as re-expression of an ORP5 deletion mutant that has lost

742   its localization to ER-PM contact sites completely rescues the levels of SAM50-VDAC.

743   Intriguingly, our data support the hypothesis that this novel function of ORP5 in

744   regulating levels of SAM50 and VDAC (and consequently mitochondrial Ca^{2+} uptake)

745   could be dependent on its direct function in mediating PS transport to mitochondria for

746   synthesis of mitochondrial PE. This is consistent with the lack of effect of ORP8

30

747   knockdown (that alone does not induce a significant decrease in mitochondrial PE) on

748   SAM50-VDAC and mitochondrial Ca^{2+} levels and with the increase in SAM50-VDAC

749   levels in cells knocked down for PISD, the enzyme that converts PS in PE on

750   mitochondria. The present data are also in accord with a previous work showing that

751   lack of mitochondrial PE by depleting Psd1/2 in yeast induced stabilization and even

752   appearance of higher forms of respiratory chain supercomplexes (Bottinger, Horvath

753   et al., 2012). Importantly, double-knockdown of ORP5 and VDAC rescues the

754   mitochondrial Ca^{2+} increase induced by ORP5 silencing, confirming that this increase in

755   Ca^{2+} is indeed VDAC-dependent. Mitochondrial membrane potential has been proposed

756   to influence VDAC open-closed state and consequently import of Ca^{2+} to mitochondria

757   (Tan & Colombini, 2007). However, we did not detect any alteration in mitochondria

758   membrane potential in ORP5 knockdown cells, supporting our idea that the increase in

759   mitochondrial Ca^{2+} observed in ORP5-silenced cells results from the increase in VDAC

760   protein levels. This is also in accord with previous studies showing that the

761   overexpression of VDAC in HeLa cells enhances mitochondrial Ca^{2+} uptake upon

762   histamine treatment (Rapizzi et al., 2002). Our data also indicate that the effect of

763   VDAC accumulation on mitochondrial Ca^{2+} fluxes does not depend on the modification

764   of ER Ca^{2+} storage or release. Indeed, we observed a similar decrease of ER Ca^{2+} in

765   ORP5 depleted and control cells, upon histamine treatment. Our results correlate well

766   with those of others (Rapizzi et al., 2002) who also observed a similar decrease of ER

767   Ca^{2+} in VDAC-overexpressing and control cells.

768   Accumulation of Ca^{2+} in mitochondria, induced by release of Ca^{2+} from the ER

769   through IP3R channel, was recently shown to be involved in cellular senescence in

770   normal cells (Martin & Bernard, 2018, Wiel et al., 2014). Interestingly, we found that

771   knockdown of ORP5, but not ORP8, induces cellular senescence in MCR5 cells.

772   These findings are highly relevant because ORP5 overexpression has been

773   associated with several tumors (Du, Turner et al., 2017). We also show that double-

774   knockdown of ORP5 and SAM50 restores the levels of VDAC protein, as well as of

775   mitochondrial Ca^{2+}, and enables cells to escape the senescence induced by ORP5

776   depletion. These data confirm that all the above phenotypes are dependent on SAM50,

777   and possibly on its known role in the biogenesis of VDAC (Hohr et al., 2018). Future

778   studies are required to further dissect the mechanisms underlying the role of ORP5 in

779   modulating SAM50 protein levels in mitochondria.

780   In conclusion, our data reveal that: 1) ORP5/8 constitute the molecular machinery

781   mediating PS transfer at ER-mitochondria contact sites but not ER-mitochondria

782   tethering; 2) ER-mitochondria contacts where ORP5/8 localize are physically associated

783   with intra-mitochondrial contacts to facilitate the transport of PS from the ER to

784   mitochondria membranes; 3) ORP5 plays a novel specific role in regulating

785   mitochondrial Ca^{2+} fluxes at ER-mitochondria contact sites via SAM50/VDAC (Fig. 8)

786   and cellular senescence in MCR5 cells. Our study uncovers a novel link between lipid

787   and Ca^{2+} transport at ER-mitochondria contact sites and provides a first molecular clue

788   on how lipids are transported at ER-mitochondria contact sites. Furthermore, we

789   reveal a specific role of ORP5 in regulating mitochondrial Ca^{2+} homeostasis and

790   cellular senescence in mammalian cells.

791

792

793

794

795

796

32

797   **METHODS**

798   **Cell culture, siRNA and transfection**.

799   HeLa cells were cultured in DMEM (Life Technologies) containing GlutaMax (Life

800   Technologies) and supplemented with 10% FBS (Life Technologies) and 1%

801   penicillin/streptomycin (Life Technologies) at 37°C and 5% CO_2. Transfection of

802   plasmids and siRNA oligos (Dharmacon, GE Healthcare) was carried out with

803   lipofectamine 2000 and oligofectamine (Life Technologies) according to

804   manufacturer's instructions.

805   For senescence studies, MRC5 normal human fibroblasts (ATCC) were cultured in

806   Dulbecco's modified Eagle's medium (Life Technologies) containing GlutaMax (Life

807   Technologies) and supplemented with 10% FBS (Sigma-Aldrich) and 1%

808   penicillin/streptomycin (Life Technologies). MRC5 were transfected with siRNAs

809   using Dharmafect 1 transfection reagent according to manufacturer's instructions

810   (Dharmacon, GE Healthcare).

811

812   **siRNAs oligonucleotides**

813   For knockdowns, HeLa cells were transfected with siRNA oligos by using

814   oligofectamine (Life Technologies) and cultured for 48 hours prior to analysis.

815   For senescence studies, MRC5 cells were transfected with siRNAs using Dharmafect

816   1 transfection reagent according to manufacturer's instructions (Dharmacon, GE

817   Healthcare).

818   Double-stranded siRNAs were derived from the following references:

siRNA	Company, Reference
OSBPL8	Dharmacon, J-009508-06 (Galmes et al., 2016)
OSBPL8	Dharmacon, J-009508-05 (Galmes et al., 2016)

33

OSBPL5	Dharmacon, J-009274-10 (Galmes et al., 2016)
OSBPL5	Dharmacon, J-009274-11 (Galmes et al., 2016)
SAMM50	Dharmacon, J-017871-18
SAMM50	Dharmacon, J-017871-19
Non-targeting	Dharmacon, D-001810-10
hVDAC1	5'-AAGCGGGAGCACATTAACCTG-3' (De Stefani, Bononi et al., 2012)
hVDAC2	5'-AAGGATGATCTCAACAAGAGC-3' (De Stefani et al., 2012)
VDAC3	5'-AAGGGTGGCTTGCTGGCTATC-3' (De Stefani et al., 2012)
siMitofilin	5' -AAUUGCUGGAGCUGGCCUUTT-3' (John, Shang et al., 2005)
siPISD	5' -GGAAGGGAAUGAGCUCUAUCACU -3' (si PISD "C" Origene)

819

Plasmids and cDNA clones

821 EGFP-ORP5, EGFP-ORP8, EGFP-ORP5ΔPH, EGFP-ORP8ΔPH, EGFP-

822 ORP5ΔORD and EGFP-ORP5ΔTM were described in (Galmes et al., 2016).

823 The following reagents were kind gifts: GFP-Sec61β from T. Rapoport (Harward

824 University)(Shibata, Voss et al., 2008), 2mt RP ratiometric Pericam from Paolo

825 Pinton (University of Ferrara) (Filippin, Abad et al., 2005); ssHRP-KDEL from T.

826 Schikorski (Schikorski, Young et al., 2007); GST-ORD8 (ORD ORP8, corresponding

827 to aa 328-767) from P. De Camilli (Chung et al., 2015). GECO constructs were from

828 Robert Campbell (Addgene: CMV-R-GECO1 # 32444, CMV-mito-R-GECO1 # 46021,

829 CMV-ER-LAR-GECO1 # 61244, CMV-mito-LAR-GECO1.2 # 61245).

830

831 **Cloning of HA-ORP5, HA-SAM50, Mitofilin-GFP, GST- ORD5 (ORD ORP5) and**

832 **EGFP-ORP5is2**

34

833   cDNAs of ORP5 (full-length), SAM50 (full-lenght), Mitoflin (full-length from FLAG-

834   mitofilin (Ott et al., 2015)) and GST-ORD5 (corresponding to aa 265-703), were

835   amplified by PCR. In all PCR reactions, Herculase II fusion DNA polymerase

836   (Agilent) was used. Primers used were (coding sequence shown in lowercase):

837   5' AgeI-HA-ORP5_Fw GGCGGC *ACCGGT* cgccacc ATGTACCCATACGATGTTCCA

838   GATTACGCT atgaaggaggaggccttcctc

839   3' XhoI-STOP-ORP5_Rv GGC *CTCGAG* ctatttgaggatgtggttaatg

840   5' AgeI-SAMM50_Fw GGCGGC *ACCGGT*cgccaccatggggactgtgcacgcccggagtttg 3'

841   5' XhoI-STOP-HA-SAMM50_Rv GGC*CTCGAG*ctaAGCGTAATCTGGAACATCGTAT

842   GGGTAcaggaaccttatcccagctccaaac 3'

843   5' KpnI-Mitofilin_Fw AGACCCAAGCTT *GGTACC* atg

844   3' BamHI-GC-Mitofilin_Rv GTAATC *GGATTC* GC ctctggct

845   5' SalI-TC-ORD5_Fw GCACAG GTCGAC TC gagacccctggggccccggt

846   3' NotI-STOP-ORD5_Rv GCACA *GCGGCCGC* ctactgtggccggagggctggtcg

847   For the HA-ORP5 cloning the PCR product (carrying the HA tag at the N-terminus of

848   ORP5) was ligated between AgeI and XhoI in the pEGFP-C1 vector (Clontech) and

849   replacing the GFP- with the HA-tag. For the SAMM50-HA cloning the PCR product

850   (carrying the HA tag at the C-terminus of SAM50) was ligated between AgeI and

851   XhoI in the pEGFP-C1 vector (Clontech) and replacing the GFP- with the HA-tag. For

852   the other clonings the PCR products were ligated between KpnI and BamHI for

853   Mitofilin, and between SalI and NotI for ORD5, in the pEGFP-N1 vector (Clontech) to

854   generate Mitofilin-EGFP or in the pGEX-6P-1 to generate GST-ORD5.

855   The ORP5is2, carrying a deletion (residues 134-201) in the PH domain, was

856   generated by sites directed mutagenesis using the following primers: sense 5'-

857   tggctgacagcctgaagggcccccaaagg-3' and antisense 5'-cctttggggcccttcaggctgtcagcca-3'.

858   PCR was carried out using PFU ultra high fidelity (Agilent), followed by 5 hrs

859   digestion with DpnI.

860

861   **mRNA analyses by quantitative reverse transcriptase PCR (qPCR)**

862   Total RNA was isolated from HeLa cells transfected with siRNAs for 48 hours as

863   described above, by using a Purelink™ kit (Ambion/Thermo Scientific, Foster City,

864   CA). The RNA (0.5 μg per specimen) was reverse transcribed with a SuperScript

865   VILO™ cDNA synthesis kit (Invitrogen/Thermo Scientific, Carlsbad, CA) according to

866   the manufacturer's protocol. Quantification of the mRNAs of interest was carried out

867   on a Roche Lightcycler™ 480 II instrument by using SYBR-Green I Master mix

868   (Roche, Basel, Switzerland) and primers specified in Table SX. Succinate

869   dehydrogenase complex. subunit A, the mRNA of which remained markedly stable

870   under the present conditions, was employed as a reference housekeeping mRNA.

871   Relative mRNA levels were calculated by using the $-\Delta\Delta$Ct method.

872   Sequences of the primers used for qPCR:

mRNA	Sequence 5'-3'
SDHA* (housekeeping)	Fw: CATGCTGCCGTGTTCCGTGTGGG
	Rv: GGACAGGGTGTGCTTCCTCCAGTGCTCC
ORP5	Fw: GTGCCGCTGGAGGAGCAGAC
	Rv: AGGGGCTGTGGTCCTCGTATC
SAMM50	Fw: CAAGTGGACCTGATTTTGGAGG
	Rv: AGACGGAGCAATTTTTCACGG
Mitofilin	Fw: GTTGTATCTCAGTATCATGAGCTGG
	Rv: GTTCAGCTGATCAATACGACGA
VDAC1	Fw: ACGTATGCCGATCTTGGCAAA
	Rv: TCAGGCCGTACTCAGTCCATC
VDAC2	Fw: GCTACAGGACTGGGGACTTC
	Rv: AATGCCAAAACGAGTGCAGTT

| VDAC3 | Fw: GTAAATAATGCCAGCCTGATTG |
| | Rv: CTTCCAGGGACAAATCTGATG |

873 *succinate dehydrogenase complex, subunit A

874

875 For senescence studies, MCR5 cells RNAs were extracted using RNA Extracol lysis

876 buffer (Dutscher). cDNAs were synthesized from total RNA using the Maxima first

877 strand cDNA synthesis kit (Life Technologies). Quantitative PCR mixture contained

878 cDNA, TaqMan mix (Roche), 100 µM of a Universal Probe Library probe (Roche) and

879 200 nM of primers (Sigma-Aldrich) according to manufacturer's instructions. qPCRs

880 were carried out on a FX96 Thermocycler (Bio-Rad). qPCR reactions were as

881 follows: 95°C 10 min, followed with 40 cycles of 95°C 10s, 59°C 30s. The reactions

882 were performed at least in duplicate. The relative amount of mRNA (ORP5, p16, p21,

883 Ki67, PGK1 and HPRT1) was calculated using the comparative Ct (ΔΔCt) method

884 and data were normalized using two housekeeping genes (PGK1 and HPRT1).

885

886 Sequences of the primers and UPL probes used for qPCR:

mRNA/UPL probe	Sequence 5'-3'
CDKN2A (p16) / UPL 34	Fw: GTGGACCTGGCTGAGGAG
	Rv: CTTTCAATCGGGGATGTCTG
p21(CDKN1A) / UPL 32	Fw: TCACTGTCTTGTACCCTTGTGC
	Rv: GGCGTTTGGAGTGGTAGAAAT
Ki67 / UPL 32	Fw: TCAAGGAACTGATTCAGGAGAAG
	Rv: GTGCACTGAAGAACACATTTCC
ORP5 / UPL 17	Fw: GTTGTATCTCAGTATCATGAGCTGG
	Rv: GTTCAGCTGATCAATACGACGA
PGK1 / UPL probe 67	Fw: CAGCTGCTGGGTCTGTCAT
	Rv: GCTGGCTCGGCTTTAACC
HPRT1 / UPL probe 73	Fw: TGACCTTGATTTATTTTGCATACC

		Rv: CGAGCAAGACGTTCAGTCCT

887

888

889 **Antibodies, dyes and reagents list**

890 Primary antibodies used in this study were:

	Antibody	Company & Reference
WB	IP3R-3	BD Transduction Laboratories, 610312
WB	ORP5	SIGMA, HPA038712
WB	ORP5	SIGMA, HPA058727
WB	beta-Actin	Abcam, ab8226
WB	ORP8	GeneTex, GTX121273
IF, WB	SAMM50	SIGMA, HPA034537
WB	Mitofilin	Proteintech, 10179-1-AP
WB	VDAC1	Abcam, ab15895
WB	Cytochrome C	BD Pharmingen, 556433
WB	Total OXPHOS CV-ATP5A	Abcam, ab110413
WB	PDI	GeneTex, GTX30716
WB	VAPB	SIGMA, HPA013144
WB	PSS1 (PTDSS1)	SIGMA, HPA016852
WB	PISD	SIGMA,HPA031090
IF, WB	GFP	Roche, 11814460001
IEM	GFP	Life technologies, A11122
IEM	PDI	Genetex, GTX30716
IF	HA	SIGMA, H3663
IF	Cleaved caspase-3	Cell Signaling, 9661
IF	FLAG M2	SIGMA, F1804

IF	MitoTracker® Red CMXRos	M7512, Invitrogen
IF	MitoTracker® Deep Red FM	M22426, Invitrogen
IF	HA	SIGMA, H3663
IF	Cleaved caspase-3	Cell Signaling, 9661

891

Biochemical analyses

Western blot

For immunoblotting, cells were resuspended in lysis buffer [50 mM Tris, 150 mM NaCl, 1% Triton X-100, 10 mM EDTA, pH 7.2, and protease inhibitor cocktail (Roche)]. Cell lysates were then centrifuged at 21 000 g for 20 min at 4°C. The supernatants were boiled in reducing SDS sample buffer and proteins were separated using 10% SDS-PAGE and immunoblot was carried using standard methods.

For Western blot quantification, bands of protein of interest were detected using ChemiDoc™ Imaging Systems (Life Science Research, Bio-Rad) and analyzed using Image Lab™ Software. All data are presented as mean ±SEM of three experimental replicates.

Immunoprecipitation of ORPs

HeLa cells transfected with EGFP-tagged ORPs were washed in cold PBS and lysed on ice in lysis buffer [50 mM Tris, 120 mM NaCl, 40 mM Hepes, 0,5% digitonin, 0,5% CHAPS, pH 7.36, and protease inhibitor cocktail (Roche). Cell lysates were then centrifuged at 21 000 g for 20 min at 4°C. Supernatants were then incubated with Chromotek GFP-trap agarose beads (Allele Biotech) for 1 hour at 4°C under rotation. Subsequently beads were washed in 0.1 M phosphate buffer. After extensive washes in cold lysis buffer, immunoprecipitated proteins bound to the beads were processed

912   for Mass Spectrometry analysis (see below) or incubated in sample buffer (containing

913   2% SDS) and then boiled for 1 min. In the latter case immunoprecipitates were

914   loaded and separated in 10% SDS–PAGE gel and immunoblotting was carried out.

915   ***Cell fractionation***

916   HeLa cells (100×10^6 cells) were harvested 48 hours after transfection with siRNA

917   oligos and washed with PBS by centrifugation at 600 g for 5 min. The cell pellet was

918   resuspended in starting buffer (225 mM mannitol, 75 mM sucrose and 30 mM Tris-

919   HCl pH 7.4) and homogenized using a Tissue Grinder Dura-Grind®, Stainless Steel,

920   Dounce (Wheaton). The homogenate was centrifuged three times at 600 g for 5 min

921   to remove nuclei and unbroken cells. The crude mitochondria was pelleted by

922   centrifugation at 10 000 g for 10 min. To separate MAM and pure mitochondria

923   fractions, the pellet was resuspended in MRB buffer (250 mM mannitol, 5 mM

924   HEPES and 0.5 mM EGTA, pH 7.4) and layered on top of different concentrations of

925   Percoll gradient (225 mM mannitol, 25 mM HEPES, 1 mM EGTA pH 7.4 and 30% or

926   15% Percoll). After centrifugation at 95 000 g for 30 min, two dense bands containing

927   either the pure mitochondria or MAM fraction were recovered and washed twice with

928   MRB buffer by centrifugation at 6300 g for 10 min to remove residual Percoll and

929   residual contamination. MAM was pelleted by centrifugation at 100 000 g for 1 hour.

930   MAMs and pure mitochondria pellets were resuspended in Lysis Buffer (50 mM Tris,

931   150 mM NaCl, 1% Triton X-100, 10 mM EDTA, pH 7.2, and protease inhibitor

932   cocktail) and protein concentrations were determined by Bradford assay. Equal

933   amount of proteins were loaded on 4-20% gradient SDS-PAGE gels (Biorad) and

934   immunoblotting was carried out. Pure mitochondria were processed for MS-lipidomic

935   analysis (see below).

936   ***Mass spectrometry-proteomic analysis***

937 Mass Spectrometry (MS) analysis was carried out by the proteomics/mass

938 spectrometry platform in IJM (http://www.ijm.fr/plateformes/spectrometrie-de-masse).

939 Briefly, after washes with binding buffer, immunoprecipitations beads were rinsed

940 with 100 µl of NH4HCO3 25 mmol/l. Proteins on beads were digested overnight at

941 37°C by sequencing grade trypsin (12,5 µg/ml; Promega Madison, Wi, USA) in 20 µl

942 of NH4HCO3 25 mmol/l. Digests were analysed by an Orbitrap Fusion (Thermo

943 Fisher Scientific, San Jose, CA) equipped with a Thermo Scientific EASY-Spray

944 nanoelectrospray ion source and coupled to an Easy nano-LC Proxeon 1000 system

945 (Thermo Fisher Scientific, San Jose, CA). MS/MS data were processed with

946 Proteome Discoverer 1.4 software (Thermo Fisher scientific, San Jose, CA) coupled

947 to an in house Mascot search server (Matrix Science, Boston, MA ; version 2.4.2).

948 MS/MS datas were searched against SwissProt databases with Homo sapiens

949 taxonomy.

950

951 **Mass Spectrometry-lipidomic analysis**

952 700 µl of homogenized cells were mixed with 800 µl 1 N $HCl:CH_3OH$ 1:8 (v/v), 900 µl

953 $CHCl_3$ and 200 µg/ml of the antioxidant 2,6-di-tert-butyl-4-methylphenol (BHT; Sigma

954 Aldrich). The organic fraction was evaporated using a Savant Speedvac spd111v

955 (Thermo Fisher Scientific). Lipid pellets were reconstituted in running solution

956 ($CH_3OH:CHCl_3:NH_4OH$; 90:10:1.25; v/v/v). Phospholipid species were analyzed by

957 electrospray ionization tandem mass spectrometry (ESI-MS/MS) on a hybrid triple

958 quadrupole/linear ion trap mass spectrometer (4000 QTRAP system; Applied

959 Biosystems SCIEX) equipped with a TriVersa NanoMate (Advion Biosciences)

960 robotic nanosource. Phospholipid profiling was executed by (positive or negative)

961 precursor ion or neutral loss scanning at a collision energy of 35 eV for neutral loss

962 141 (phosphatidylethanolamine (PE)). Phospholipid quantification was performed by

963 multiple reaction monitoring (MRM), the transitions being based on the neutral losses

964 or the typical product ions as described above. The MRM dwell time was set to 100

965 ms and typically the signal was averaged over 20 cycles. Lipid standards used were

966 PE25:0 and PE43:6 (Avanti Polar Lipids). The data were corrected for isotope effects

967 as described by (Liebisch, Lieser et al., 2004).

968

969 **Lipid Transfer assay**

970 ***ORP5 and ORP8 ORD domain purification***

971 Escherichia coli BL21DE3 RILP (Invitrogen) cells were transformed with plasmids

972 encoding for GST tagged ORP5 or ORP8 ORD domains following the manufacturer's

973 instruction. Bacteria were then grown overnight at 37°C and used to inoculate a

974 large-scale volume (1L). When the OD_{600} reached 0.4, cultures were cool down and

975 incubate at 18°C until they reached O_{D600} = 0.65. Cells were induced by addition

976 of isopropyl β-D-1-thiogalactopyranoside to a final concentration of 0.1 mM and were

977 incubated overnight at 18°C before harvesting. Cells were resuspended in 35 ml

978 binding buffer (1X PBS, 1 mM EDTA, 1 mM DTT, Protease inhibitor) then 250 units

979 of benzonase nuclease (Sigma) were added to the resuspension. Cells were lysed by

980 sonication and the supernatant was recover after 20 min centrifugation at 184 000g

981 and 4°C. Supernatant containing GST tagged proteins was incubated with 2 ml of

982 Glutathione Sepharose 4 fast flow for 1 hour at 4°C under nutation. Beads were

983 washed using a serie of wash buffer: 1st (1X PBS, 1 mM EDTA, 1 mM DTT), 2nd HSP-

984 removal buffer (50 mM Tris pH7.5, 50 mM KCl, 20 mM MgCl2, 5 mM ATP) then

985 cleavage buffer (50 mM Tris pH 7.5, 150 mM NaCl, 1 mM EDTA, 1 mM DTT).

986 Cleavage of the GST tag was realized overnight at 4°C using Prescission protease.

987 Untagged proteins were eluted with cleavage buffer, flash frozen and stored at -80°C

988 until lipid transfer assay was performed.

989 ***Lipids***

990 1-palmitoyl-2-oleoyl-sn-glycero-3-phosphocholine (POPC), 1,2-dioleoyl-sn-glycero-3-

991 phosphoethanolamine-N-(cap biotinyl) (Biotinyl Cap PE), 1-palmitoyl-2-

992 (dipyrrometheneboron difluoride)undecanoyl-sn-glycero-3-phosphoethanolamine

993 (TopFluor-PE), 1-palmitoyl-2-(dipyrrometheneboron difluoride)undecanoyl-sn-

994 glycero-3-phospho-L-serine (TopFluor-PS), 1-palmitoyl-2-(dipyrrometheneboron

995 difluoride)undecanoyl-sn-glycero-3-phosphocholine (TopFluor-PC) were purchased

996 from Avanti Polar Lipids as chloroform solutions.

997 ***Liposome preparation***

998 1 μmol of the appropriate lipid mixtures in chloroform solution was dried in glass

999 tubes for 10 min under a gentle stream of argon, and then for 1 hour under vacuum.

1000 The dried lipid films were resuspended in 1 ml of buffer H (25 mM HEPES/KOH, pH

1001 7.7; 150 mM KCL; 10% Glycerol) by vigorously vortexing for 30 min at room

1002 temperature. Unilamellar liposomes were produced by seven freeze-thaw cycles (30

1003 sec in liquid nitrogen followed by 5 min in a 37°C water bath) and extrusion (at least

1004 21 times) through a polycarbonate filter with 100 nm pore size (polycarbonate

1005 membranes from Avanti Polar Lipids). The liposomes were then stored on ice.

1006 ***Lipid Transfer assay in vitro***

1007 The lipid transfer assays were realized with liposomes prepared as described above.

1008 The donor liposomes contained 1% mol TopFluor lipids (-PS, -PC or -PE) and 2%

1009 mol of Biotinyl Cap PE. The acceptor liposomes contained only POPC. For each

1010 reaction, 25μL of streptavidin-coated magnetic beads (DynabeadsMyOne

1011 Streptavidin T1, Invitrogen) were washed in buffer H and mixed with 25μL of 1 mM

1012   donor liposomes. The mixture was incubated for 1 hour at 25°C with intermittent

1013   gentle mixing. Bead-bound donor liposomes were then washed, resuspended in

1014   25µL and mixed with 25µL of 1 mM acceptor liposomes and 50µL of buffer H or

1015   protein (0.3 µM protein and 2.5 µM TopFluor lipids in the reaction solution). The

1016   mixture was incubated at 37°C for 1 hour with intermittent gentle mixing. Supernatant

1017   containing acceptor liposomes was recovered after binding of bead-bound donor

1018   liposomes to a magnetic rack. TopFluor fluorescence of acceptor and donor

1019   liposomes was measured (after solubilization with 0.4% (w/v) n-dodecyl-β-D-

1020   maltoside, DDM) in a SpectraMax M5 plate reader (Molecular Device) equilibrated to

1021   30°C (excitation: 450 nm; emission: 510 nm; cutoff: 475 nm; low gain). The

1022   percentage of lipids transferred from donor to acceptor liposomes was determined

1023   using the following formula: $100*F_{acceptor}/(F_{acceptor}+F_{donor})$. To confirm that

1024   fluorescence was transferred to acceptor liposomes, a fraction of the reaction

1025   supernatant – which has not been solubilized with DDM – was floated on a Nycodenz

1026   density gradient. 50 µL of supernatant was mixed with 100 µL of buffer H and 150 µL

1027   of Nycodenz 80% in buffer H. The solution was transferred to a 0.8 mL Ultra-Clear

1028   centrifuge tube (Beckman Coulter) and overlaid with 250 µL of Nycodenz 30% in

1029   buffer H and 75 µL of buffer H. The tubes were centrifuged in a SW 55 Ti rotor

1030   (Beckman Coulter) at 246,000 g for 4 hours at 4 °C. 50 µL were collected from the

1031   top of the gradient and the fluorescence was measured.

1032

1033   **Radiometric assay for the conversion of PS to PE**

1034   Hela cells were seeded on 6-well plates and transfected for 48 hours with the non-

1035   targeting, ORP5 or ORP8-specific siRNAs specified above by using Oligofectamine

1036   (Thermo Fisher Scientific). The cells were then washed and shifted into Hanks

44

1037 balanced salt solution (Gibco) supplemented with a serine-free MEM amino acid

1038 mixture and MEM vitamins (Gibco), followed by 18 hours labeling with 2 μl/well L-

1039 [^{3}H(G)]serine (30.9 Ci/mmol, NET24800, Perkin-Elmer)(Fig. 1e). In parallel

1040 experiments (Fig. 1f) cells were starved in serum-free medium for 10 hours and then

1041 treated with 1mM β-chloro-L-alanine (SIGMA) for 2 hours or left in serum-free

1042 medium, followed by 1hr pulse with 15 µCi/ml of [^{3}H(G)]serine and 12 hours chase in

1043 serum-free DMEM. After the labeling (Fig. 1e) or the chase (Fig. 1f), the cells were

1044 scraped into 0.9 ml 2% NaCl per well, a 0.1 ml aliquot was withdrawn for protein

1045 analysis with the BCA assay (Thermo Fisher Scientific), and, after adding 50 nmol of

1046 unlabeled PS as carrier, the remaining 0.8 ml was subjected to lipid extraction by an

1047 acid modification of the Folch method (Kim, Song et al., 2017). After drying, the lipids

1048 were resolved in 50 μl CHCl$_3$ and applied on Merck TLC Silica gel 60^{TM} plates,

1049 followed by separation by using CHCl$_3$-methanol-acetic acid-H2O (50:30:8:3.5) as

1050 solvent. The PS and PE spots identified from the mobility of standards run on the

1051 same plates were scraped into scintillation vials for analysis of [^{3}H] radioactivity. The

1052 DPM values were corrected for total cell protein, and the ratio of [^{3}H] in PE vs. PS

1053 calculated.

1054

1055 **Mitochondrial respiration assay**

1056 Oxygen Consumption rate (OCR) was measured using the XF$_p$ Extracellular Flux

1057 Analyzer (Seahorse Bioscience Inc.). HeLa cells were seeded on a 6-well plate 3

1058 days before the Seahorse experiment and knockdown of the proteins of interest was

1059 realized 2 days before. The day after the knockdown, HeLa cells transfected with

1060 Ctrl, ORP5, ORP8 or ORP5 and ORP8 siRNAs were plated in a Seahorse XFp 8-

1061 mini wells microplate. 20,000 HeLa cells were seeded in each well (except in the

1062　blank wells used for the background correction) in 180 µl of culture medium, and

1063　incubated overnight at 37℃ in 5% CO2. One day after, the culture medium was

1064　replaced with 180 µl of XF DMEM Medium Solution pH 7.4 and then the 8-mini wells

1065　microplate was moved in a 37°C non-CO2 incubator before measurement. OCR was

1066　determined before drug additions and after addition of Oligomycin (1.5 µM), Carbonyl

1067　cyanide 4-(trifluoromethoxy) phenylhydrazone (FCCP, 0.5 µM), and

1068　Rotenone/Antimycin A (0.5 µM) (purchased from Agilent). After each assay, all the

1069　raw OCR data were analyzed using WAVE software.

1070

1071　**Fluorescence Microscopy**

1072　***Immunofluorescence and Confocal Microscopy***

1073　HeLa cells were seeded on 13 mm glass bottom coverslips (Agar Scientific).

1074　Immunofluorescence was carried out one day after transfection. Transfected cells

1075　were fixed with 4% PFA/PBS for 15 min at room temperature, washed in PBS and

1076　incubated with 50 mM NH4Cl/PBS for 15 min at room temperature. After washing

1077　with PBS and blocking buffer (1% BSA/ 0,1% Saponin in PBS), cells were incubated

1078　with primary antibodies diluted in blocking buffer for 1 hour at room temperature and

1079　then with fluorescently-labeled secondary antibodies. After washing with blocking

1080　buffer and then PBS, coverslips were mounted on microscopy slides and images

1081　were acquired on Confocal inverted microscope SP8-X (DMI 6000 Leica). Optical

1082　sections were acquired with a 63x/1.4 Oil immersion objective using the LAS-X

1083　software and fluorescent pictures were collected with a PMTs GaAsP hybride camera

1084　(Hamamatsu). Images from a mid-focal plane are shown. Images were processed

1085　and fluorescence was analysed off line using Image J.

1086

1087　**Calcium (Ca^{2+}) indicators**

1088 ***Ca^{2+} intake assay using Geco constructs***

1089 HeLa cells were seeded on glass bottom ibidi chambers (µ-slide 2 wells) 3 days

1090 before imaging. Knockdown of the proteins of interest was realized 2 days before

1091 imaging, as described above. The day after knockdown, 0.8 µg of GECO plasmid

1092 were transfected with 6 µl of lipofectamine 2000/well (Invitrogen), according to the

1093 manufacturer's instructions. The day of imaging, cells were washed 4-5 hours before

1094 the imaging with fresh DMEM. Cell imaging was performed on an inverted Nikon Ti

1095 Eclipse E microscope coupled with a Spinning Disk (Yokogawa CSU-X1-A1) and

1096 cage incubator to control both temperature and CO_2 (37 °C, 5% CO2). After

1097 excitation with a 561 nm laser (Coherent, 100 mW), fluorescence from GECO

1098 constructs was detected with a 40X oil immersion objective (PLAN FLUOR; NA: 1.30;

1099 Nikon) and a Prime 95B sCMOS camera (Photometrics). Images were captured

1100 every 5 sec during 10 min. Approximatively 1 min after the start of captures,

1101 histamine was added to a final concentration of 100 µM to trigger Ca^{2+} release from

1102 intracellular stores. Image analysis was performed using Image J by measuring the

1103 fluorescence intensity over time (time-lapse) of cells expressing the GECO

1104 constructs. Histograms represent the response of the cell to the addition of histamine

1105 shown as the maximum fluorescence (Fmax) after treatment / mean fluorescence

1106 before histamine F0.

1107 ***Ratiometric Ca^{2+} imaging using a mt-Pericam construct***

1108 HeLa cells were seeded on glass bottom ibidi chambers (µ-slide 2 wells) 3 days

1109 before imaging. Knockdown of the proteins of interest was realized 2 days before

1110 imaging, as described above. The day after knockdown, 2.4 µg of mt-Pericam

1111 plasmid were transfected with 6 µl of lipofectamine 2000/well (Invitrogen), according

47

1112   to the manufacturer's instructions. The day of imaging, cells were washed 4-5 hours

1113   before the imaging with fresh DMEM.

1114   Imaging of mt-pericam was performed on an inverted Nikon Ti Eclipse Eclipse-E

1115   microscope coupled with a Spinning Disk (Yokogawa, CSU-X1-A1), a 40x CFI Plan

1116   Fluor objective (Nikon, NA 1.30, oil immersion) and a sCMOS camera (Photometrics,

1117   Prime 95B) with a binning of 2. Knock-down cells expressing pericam constructs

1118   were imaged in a controlled atmosphere (37°C, 5% CO_2). For each field of view, a

1119   time-lapse was recorded with an image every 8 sec during 10 min. Approximatively 3

1120   min after the start of captures, histamine was added to a final concentration of 100

1121   μM. For each time point mt-pericam fluorescence was collected using a 525/45

1122   bandpass filter (Semrock) after alternative excitation at 405 nm (Vortran, 100mW

1123   laser) and 488 nm (Vortran, 150mW laser). A perfect focus system (Nikon) was used

1124   to keep the focus constant along the timelapse, the whole system was driven by

1125   Metamorph (version 7.7, Molecular Devices).

1126   All the image processing and quantification was performed using a custom script in

1127   Image J. First, images were corrected for flat-field and dark noise using reference

1128   images respectively acquired on a fluorescent plastic slide (Chroma) and with no light

1129   reaching the detector. Regions of interest were also drawn on an empty area of every

1130   stack to perform a background subtraction on every image. Then hyperstacks

1131   containing two channels were registered to correct any lateral drift of the sample

1132   during the acquisition using the Image J plugin "HyperStackReg (v05)" with the

1133   "translation" algorithm. Once the stacks were processed, regions of interest were

1134   drawn around individual cells, a threshold applied (Mean) and the mean intensity of

1135   each cell recorded on each image pair along the time-lapse. For every cell the ratio

1136   488/405 was plotted along the time and only the cells with a stable ratio during the

1137   first 3 min time points and with a sharp increase observed after addition of histamine

1138   were kept for the final analysis.

1139

1140   **Flow cytometry for TMRE analysis**

1141   ***Membrane potential studies using TMRE- Mitochondrial Membrane Potential***

1142   ***Assay Kit***

1143   HeLa cells were seeded on 6-well plates 3 days before TMRE detection and the day

1144   after they were transfected for 48 hours with the non-targeting, ORP5 or ORP8-

1145   specific siRNAs specified above. The day before analysis, the medium was replaced

1146   with DMEM 10% FBS with or without 20 μM CCCP (Carbonyl cyanide m-

1147   chlorophenyl hydrazine) at 37°C and 5% CO_2 to induce mitochondrial depolarization.

1148   After 24 hours, 200 nM of TMRE in DMEM 10% FBS (Mitochondrial Membrane

1149   Potential Assay Kit, abcam ab113852) was added to cells and replaced after 30 min.

1150   Cells were kept at 37°C and 5% CO_2 for additional 15 min and then trypsinized and

1151   resuspended in DMEM (1-2x105 cells in 500 μl). TMRE was then analysed by flow

1152   cytometry.

1153   ***Flow cytometry***

1154   Multicolor flow cytometry was conducted on Beckman Coulter's CytoFLEX S

1155   cytometer. Analyses were performed using Beckman Coulter's Kaluza and CytExpert

1156   software. TMRE (Ex/Em = 549/575) was excited by a 561 nm laser and detected

1157   through a 585/542 nm filter channel. All acquisitions were made on 10 000 cells. All

1158   data are presented as mean ±SEM of three independent experimental replicates.

1159

1160   **Apoptosis assay using Cleaved-caspase-3 expression**

49

1161   HeLa cells were seeded on glass bottom 13 mm coverslips in a 24 well plates. The

1162   next day, 48 hours knockdown of the proteins of interest were realized as described

1163   above. 2 days after the knockdown, cells were treated with 1 μM staurosporine or

1164   with DMSO to induce apoptosis. After 4 hours apoptotic cells were analyzed by

1165   confocal immunofluorescence, using cleaved Caspase-3 antibody and Mitotracker

1166   red to label mitochondria. Cleaved Caspase-3 positive cells were quantified using the

1167   Cell Counter plugin from Image J Software. All data are presented as mean ±SEM of

1168   three experimental replicates.

1169

1170   **Senescence studies using SA-β-Galactosidase assay and crystal violet**

1171   **staining**

1172   For SA-β-galactosidase assay, cells were washed twice with PBS and fixed 5 min

1173   with 2% formaldehyde / 0.2% glutaraldehyde. Cells were then rinsed twice in PBS

1174   and incubated at 37°C overnight in SA-β-Gal staining solution as previously

1175   described (Itahana, Campisi et al., 2007).

1176   For crystal violet staining, cells were washed with PBS, fixed for 15 min in 3.7%

1177   formaldehyde and then stained with 0.5% crystal violet solution. After drying, plates

1178   were scanned.

1179   Relative cell count was determined by dissolving crystal violet in acetic acid solution

1180   and measuring optical density at 595 nM.

1181

1182   **Electron Microscopy Analysis**

1183   ***Conventional EM***

1184   For conventional EM, cells grown on 13 mm glass bottom coverslips (Agar Scientific)

1185   were fixed with 2.5% glutaraldehyde and 2% PFA in 0.1 M cacodylate, 0.05% $CaCl_2$

1186 buffer for 24 hours. After several washes with 0.1 M cacodylate buffer, the cells were

1187 postfixed with 1% OsO_4, 1.5% potassium ferricyanide in 0.1M Cacodylate for 1 hour.

1188 After several washes with 0.1 M cacodylate buffer and H_2O, the cells were stained

1189 with 0.5% uranyl acetate for 24 hours. After several washes with H_2O, the cells were

1190 dehydrated in ethanol and embedded in Epon while on the coverslips. Ultrathin

1191 sections were prepared, counterstained with uranyl acetate and observed under a

1192 MET JEOL 1400 equipped with a Orius High speed (Gatan) camera.

1193 ***HRP Detection***

1194 HeLa cells expressing HRP-KDEL were fixed on coverslips with 1.3% glutaraldehyde

1195 in 0.1 M cacodylate buffer, washed in 0.1 M ammonium phosphate [pH 7.4] buffer for

1196 1 hour and HRP was visualized with 0.5 mg/ml DAB and 0.005% H_2O_2 in 0.1 M

1197 Ammonium Phosphate [pH 7.4] buffer. Development of HRP (DAB dark reaction

1198 product) took between 5 min to 20 min and was stopped by extensive washes with

1199 cold water. Cells were postfixed in 2% OsO_4+1% $K_3Fe(CN)_6$ in 0.1 M cacodylate

1200 buffer at 4°C for 1 hour, washed in cold water and then contrasted in 0.5% uranyl

1201 acetate for 2 hours at 4°C, dehydrated in an ethanol series and embedded in epon as

1202 for conventional EM. Ultrathin sections were counterstained with 2% uranyl acetate

1203 and observed under a FEI Tecnai 12 microscope equipped with a CCD (SiS 1kx1k

1204 keenView) camera.

1205 ***Immunogold labelling***

1206 HeLa cells were fixed with a mixture of 2%PFA and 0.125% glutaraldehyde in 0.1 M

1207 phosphate buffer [pH 7.4] for 2 hours, and processed for ultracryomicrotomy as

1208 described previously (Slot & Geuze, 2007). Ultrathin cryosections were single- or

1209 double-immunogold-labeled with antibodies and protein A coupled to 10 or 15 nm

1210 gold (CMC, UMC Utrecht, The Netherlands), as indicated in the legends to the

1211 figures. Immunogold-labeled cryosections were observed under a FEI Tecnai 12

1212 microscope equipped with a CCD (SiS 1kx1k keenView) camera.

1213 *Quantifications*

1214 For the quantification of the number of cristae junction in Epon sections, about 200

1215 mitochondria were analyzed in randomly selected cell profiles and cristae junctions

1216 were counted in each of the mitochondria profile and reported as number of

1217 cristae/mitochondria profile. All data are presented as mean ±SEM of three

1218 experimental replicates.

1219 For the quantification of ER-mitochondria contact sites in HRP-stained Epon

1220 sections, the total circumference of each mitochondria and the length of the multiple

1221 HRP-positive ER segments closely associated (<30 nm) with them were measured

1222 by iTEM software (Olympus) on acquired micrographs of HeLa cells for each of 20-

1223 30 cell profiles, as indicated in the figure legends. Cells were randomly selected for

1224 analysis without prior knowledge of transfected plasmid or siRNA. All data are

1225 presented as mean (%) ±SEM of three experimental replicates.

1226 For the quantification of immunogold labeling on ultrathin cryosections, 150 gold

1227 particles were counted on acquired micrographs of randomly selected cell profiles at

1228 specific ranges of distance from CJ (0-50, 50-100, 100-150, 150-200 nm) in each of

1229 three experiments. All data are presented as mean (%) ±SEM of three experimental

1230 replicates.

1231 **ACKNOWLEDGEMENTS**

1251

1252

1253   **AUTHOR CONTRIBUTIONS**

1254   FG conceived and supervised the work. VO designed and supervised the radiometric

1255   assays for PS-to-PE conversion and the expression analysis by RT-PCR. DT

1256   designed and supervised the *in vitro* lipid transfer assays. DB designed and

1257   supervised the senescence assays including part of the RT-PCR analysis. LR and

1258   CS performed and analyzed the cell experiments including Ca^{2+} imaging. LR, AH,

1259   and FG performed and analyzed the EM experiments. CS, AH and DT performed

1260   and analyzed the *in vitro* lipid transfer assays. EJ, AA and AK performed and

1261   analyzed the radiometric assays for PS-to-PE conversion. EM, JD and JS performed

1262   MS-lipidomic analysis. RLB provided tools and techniques for Ca^{2+} imaging analysis.

1263   JN provided technical help and generated some of the constructs for mammalian cell

1264   expression. XM performed the senescence experiments. LR, CS and FG wrote the

1265   manuscript and all authors commented on the manuscript.

1266

1267   **DECLARATION OF INTERESTS**

1268   The authors declare that they have no competing interests.

1269

1270

1271

1272   **REFERENCES**

1273   Aaltonen MJ, Friedman JR, Osman C, Salin B, di Rago JP, Nunnari J, Langer T, Tatsuta T
1274   (2016) MICOS and phospholipid transfer by Ups2-Mdm35 organize membrane lipid
1275   synthesis in mitochondria. The Journal of cell biology 213: 525-34
1276   Bottinger L, Horvath SE, Kleinschroth T, Hunte C, Daum G, Pfanner N, Becker T (2012)
1277   Phosphatidylethanolamine and cardiolipin differentially affect the stability of
1278   mitochondrial respiratory chain supercomplexes. Journal of molecular biology 423: 677-
1279   86
1280   Chen H, Born E, Mathur SN, Field FJ (1993) Cholesterol and sphingomyelin syntheses are
1281   regulated independently in cultured human intestinal cells, CaCo-2: role of membrane
1282   cholesterol and sphingomyelin content. J Lipid Res 34: 2159-67
1283   Chung J, Torta F, Masai K, Lucast L, Czapla H, Tanner LB, Narayanaswamy P, Wenk MR,
1284   Nakatsu F, De Camilli P (2015) INTRACELLULAR TRANSPORT. PI4P/phosphatidylserine
1285   countertransport at ORP5- and ORP8-mediated ER-plasma membrane contacts. Science
1286   349: 428-32
1287   Colombini M (2012) VDAC structure, selectivity, and dynamics. Biochimica et biophysica
1288   acta 1818: 1457-65
1289   De Stefani D, Bononi A, Romagnoli A, Messina A, De Pinto V, Pinton P, Rizzuto R (2012)
1290   VDAC1 selectively transfers apoptotic Ca2+ signals to mitochondria. Cell Death Differ 19:
1291   267-73
1292   Ding C, Wu Z, Huang L, Wang Y, Xue J, Chen S, Deng Z, Wang L, Song Z, Chen S (2015)
1293   Mitofilin and CHCHD6 physically interact with Sam50 to sustain cristae structure. Sci
1294   Rep 5: 16064
1295   Du X, Turner N, Yang H (2017) The role of oxysterol-binding protein and its related
1296   proteins in cancer. Semin Cell Dev Biol
1297   Du X, Zadoorian A, Lukmantara IE, Qi Y, Brown AJ, Yang H (2018) Oxysterol-binding
1298   protein-related protein 5 (ORP5) promotes cell proliferation by activation of mTORC1
1299   signaling. The Journal of biological chemistry 293: 3806-3818

1300 Filippin L, Abad MC, Gastaldello S, Magalhaes PJ, Sandona D, Pozzan T (2005) Improved
1301 strategies for the delivery of GFP-based Ca2+ sensors into the mitochondrial matrix. Cell
1302 calcium 37: 129-36
1303 Friedman JR, Mourier A, Yamada J, McCaffery JM, Nunnari J (2015) MICOS coordinates
1304 with respiratory complexes and lipids to establish mitochondrial inner membrane
1305 architecture. eLife 4
1306 Galmes R, Houcine A, van Vliet AR, Agostinis P, Jackson CL, Giordano F (2016)
1307 ORP5/ORP8 localize to endoplasmic reticulum-mitochondria contacts and are involved
1308 in mitochondrial function. EMBO reports 17: 800-10
1309 Ghai R, Du X, Wang H, Dong J, Ferguson C, Brown AJ, Parton RG, Wu JW, Yang H (2017)
1310 ORP5 and ORP8 bind phosphatidylinositol-4, 5-biphosphate (PtdIns(4,5)P 2) and
1311 regulate its level at the plasma membrane. Nature communications 8: 757
1312 Giordano F (2018) Non-vesicular lipid trafficking at the endoplasmic reticulum-
1313 mitochondria interface. Biochemical Society transactions 46: 437-452
1314 Guarani V, McNeill EM, Paulo JA, Huttlin EL, Frohlich F, Gygi SP, Van Vactor D, Harper JW
1315 (2015) QIL1 is a novel mitochondrial protein required for MICOS complex stability and
1316 cristae morphology. eLife 4
1317 Hanada K, Nishijima M, Kiso M, Hasegawa A, Fujita S, Ogawa T, Akamatsu Y (1992)
1318 Sphingolipids are essential for the growth of Chinese hamster ovary cells. Restoration of
1319 the growth of a mutant defective in sphingoid base biosynthesis by exogenous
1320 sphingolipids. The Journal of biological chemistry 267: 23527-33
1321 Harner M, Korner C, Walther D, Mokranjac D, Kaesmacher J, Welsch U, Griffith J, Mann M,
1322 Reggiori F, Neupert W (2011) The mitochondrial contact site complex, a determinant of
1323 mitochondrial architecture. The EMBO journal 30: 4356-70
1324 Heikinheimo L, Somerharju P (1998) Preferential decarboxylation of hydrophilic
1325 phosphatidylserine species in cultured cells. Implications on the mechanism of transport
1326 to mitochondria and cellular aminophospholipid species compositions. The Journal of
1327 biological chemistry 273: 3327-35
1328 Herrera-Cruz MS, Simmen T (2017) Of yeast, mice and men: MAMs come in two flavors.
1329 Biol Direct 12: 3
1330 Hirabayashi Y, Kwon SK, Paek H, Pernice WM, Paul MA, Lee J, Erfani P, Raczkowski A,
1331 Petrey DS, Pon LA, Polleux F (2017) ER-mitochondria tethering by PDZD8 regulates
1332 Ca(2+) dynamics in mammalian neurons. Science 358: 623-630
1333 Hohr AIC, Lindau C, Wirth C, Qiu J, Stroud DA, Kutik S, Guiard B, Hunte C, Becker T,
1334 Pfanner N, Wiedemann N (2018) Membrane protein insertion through a mitochondrial
1335 beta-barrel gate. Science 359
1336 Huynen MA, Muhlmeister M, Gotthardt K, Guerrero-Castillo S, Brandt U (2016) Evolution
1337 and structural organization of the mitochondrial contact site (MICOS) complex and the
1338 mitochondrial intermembrane space bridging (MIB) complex. Biochimica et biophysica
1339 acta 1863: 91-101
1340 Itahana K, Campisi J, Dimri GP (2007) Methods to detect biomarkers of cellular
1341 senescence: the senescence-associated beta-galactosidase assay. Methods Mol Biol 371:
1342 21-31
1343 John GB, Shang Y, Li L, Renken C, Mannella CA, Selker JM, Rangell L, Bennett MJ, Zha J
1344 (2005) The mitochondrial inner membrane protein mitofilin controls cristae
1345 morphology. Molecular biology of the cell 16: 1543-54
1346 Joshi AS, Thompson MN, Fei N, Huttemann M, Greenberg ML (2012) Cardiolipin and
1347 mitochondrial phosphatidylethanolamine have overlapping functions in mitochondrial
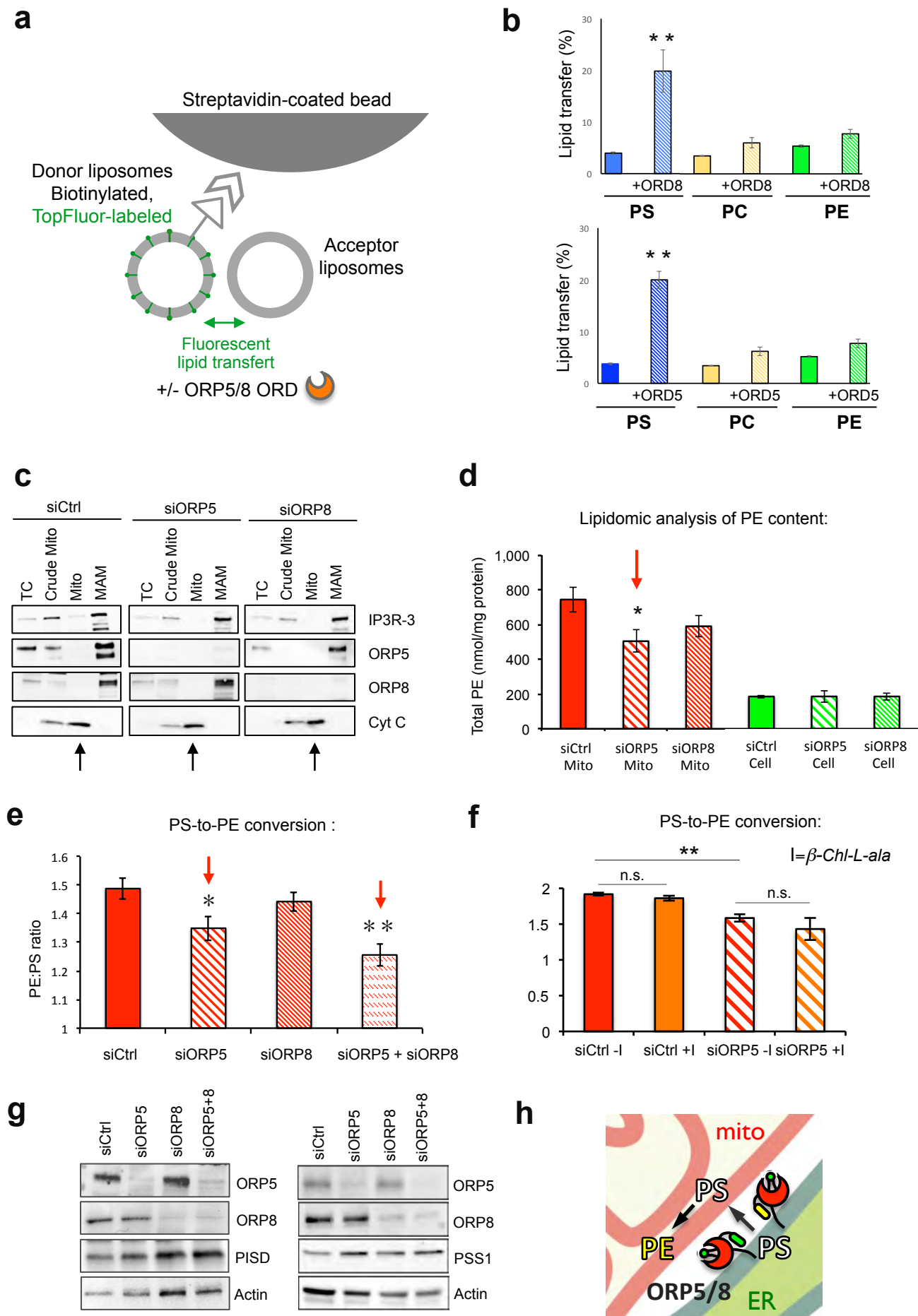1348 fusion in Saccharomyces cerevisiae. The Journal of biological chemistry 287: 17589-97

1349 Kim SH, Song HE, Kim SJ, Woo DC, Chang S, Choi WG, Kim MJ, Back SH, Yoo HJ (2017)
1350 Quantitative structural characterization of phosphatidylinositol phosphates from
1351 biological samples. J Lipid Res 58: 469-478
1352 Kopec KO, Alva V, Lupas AN (2010) Homology of SMP domains to the TULIP superfamily
1353 of lipid-binding proteins provides a structural basis for lipid exchange between ER and
1354 mitochondria. Bioinformatics 26: 1927-31
1355 Kornmann B, Currie E, Collins SR, Schuldiner M, Nunnari J, Weissman JS, Walter P (2009)
1356 An ER-mitochondria tethering complex revealed by a synthetic biology screen. Science
1357 325: 477-81
1358 Kozjak V, Wiedemann N, Milenkovic D, Lohaus C, Meyer HE, Guiard B, Meisinger C,
1359 Pfanner N (2003) An essential role of Sam50 in the protein sorting and assembly
1360 machinery of the mitochondrial outer membrane. The Journal of biological chemistry
1361 278: 48520-3
1362 Kozjak-Pavlovic V, Ross K, Benlasfer N, Kimmig S, Karlas A, Rudel T (2007) Conserved
1363 roles of Sam50 and metaxins in VDAC biogenesis. EMBO reports 8: 576-82
1364 Kumar N, Leonzino M, Hancock-Cerutti W, Horenkamp FA, Li P, Lees JA, Wheeler H,
1365 Reinisch KM, De Camilli P (2018) VPS13A and VPS13C are lipid transport proteins
1366 differentially localized at ER contact sites. The Journal of cell biology 217: 3625-3639
1367 Lang A, John Peter AT, Kornmann B (2015) ER-mitochondria contact sites in yeast:
1368 beyond the myths of ERMES. Current opinion in cell biology 35: 7-12
1369 Liebisch G, Lieser B, Rathenberg J, Drobnik W, Schmitz G (2004) High-throughput
1370 quantification of phosphatidylcholine and sphingomyelin by electrospray ionization
1371 tandem mass spectrometry coupled with isotope correction algorithm. Biochimica et
1372 biophysica acta 1686: 108-17
1373 Ma X, Warnier M, Raynard C, Ferrand M, Kirsh O, Defossez PA, Martin N, Bernard D
1374 (2018) The nuclear receptor RXRA controls cellular senescence by regulating calcium
1375 signaling. Aging Cell 17: e12831
1376 Maeda K, Anand K, Chiapparino A, Kumar A, Poletto M, Kaksonen M, Gavin AC (2013)
1377 Interactome map uncovers phosphatidylserine transport by oxysterol-binding proteins.
1378 Nature 501: 257-61
1379 Martin N, Bernard D (2018) Calcium signaling and cellular senescence. Cell calcium 70:
1380 16-23
1381 Moser von Filseck J, Copic A, Delfosse V, Vanni S, Jackson CL, Bourguet W, Drin G (2015)
1382 INTRACELLULAR TRANSPORT. Phosphatidylserine transport by ORP/Osh proteins is
1383 driven by phosphatidylinositol 4-phosphate. Science 349: 432-6
1384 Nagai T, Sawano A, Park ES, Miyawaki A (2001) Circularly permuted green fluorescent
1385 proteins engineered to sense Ca2+. Proceedings of the National Academy of Sciences of
1386 the United States of America 98: 3197-202
1387 Ott C, Dorsch E, Fraunholz M, Straub S, Kozjak-Pavlovic V (2015) Detailed analysis of the
1388 human mitochondrial contact site complex indicate a hierarchy of subunits. PloS one 10:
1389 e0120213
1390 Patron M, Raffaello A, Granatiero V, Tosatto A, Merli G, De Stefani D, Wright L,
1391 Pallafacchina G, Terrin A, Mammucari C, Rizzuto R (2013) The mitochondrial calcium
1392 uniporter (MCU): molecular identity and physiological roles. The Journal of biological
1393 chemistry 288: 10750-8
1394 Pulli I, Lassila T, Pan G, Yan D, Olkkonen VM, Tornquist K (2018) Oxysterol-binding
1395 protein related-proteins (ORPs) 5 and 8 regulate calcium signaling at specific cell
1396 compartments. Cell calcium 72: 62-69

1397 Rapizzi E, Pinton P, Szabadkai G, Wieckowski MR, Vandecasteele G, Baird G, Tuft RA,
1398 Fogarty KE, Rizzuto R (2002) Recombinant expression of the voltage-dependent anion
1399 channel enhances the transfer of Ca2+ microdomains to mitochondria. The Journal of
1400 cell biology 159: 613-24
1401 Reinisch KM, De Camilli P (2016) SMP-domain proteins at membrane contact sites:
1402 Structure and function. Biochimica et biophysica acta 1861: 924-927
1403 Rizzuto R, Marchi S, Bonora M, Aguiari P, Bononi A, De Stefani D, Giorgi C, Leo S, Rimessi
1404 A, Siviero R, Zecchini E, Pinton P (2009) Ca(2+) transfer from the ER to mitochondria:
1405 when, how and why. Biochimica et biophysica acta 1787: 1342-51
1406 Schikorski T, Young SM, Jr., Hu Y (2007) Horseradish peroxidase cDNA as a marker for
1407 electron microscopy in neurons. Journal of neuroscience methods 165: 210-5
1408 Scorrano L, De Matteis MA, Emr S, Giordano F, Hajnoczky G, Kornmann B, Lackner LL,
1409 Levine TP, Pellegrini L, Reinisch K, Rizzuto R, Simmen T, Stenmark H, Ungermann C,
1410 Schuldiner M (2019) Coming together to define membrane contact sites. Nature
1411 communications 10: 1287
1412 Shiao YJ, Lupo G, Vance JE (1995) Evidence that phosphatidylserine is imported into
1413 mitochondria via a mitochondria-associated membrane and that the majority of
1414 mitochondrial phosphatidylethanolamine is derived from decarboxylation of
1415 phosphatidylserine. The Journal of biological chemistry 270: 11190-8
1416 Shibata Y, Voss C, Rist JM, Hu J, Rapoport TA, Prinz WA, Voeltz GK (2008) The reticulon
1417 and DP1/Yop1p proteins form immobile oligomers in the tubular endoplasmic
1418 reticulum. The Journal of biological chemistry 283: 18892-904
1419 Slot JW, Geuze HJ (2007) Cryosectioning and immunolabeling. Nature protocols 2: 2480-
1420 91
1421 Steenbergen R, Nanowski TS, Beigneux A, Kulinski A, Young SG, Vance JE (2005)
1422 Disruption of the phosphatidylserine decarboxylase gene in mice causes embryonic
1423 lethality and mitochondrial defects. The Journal of biological chemistry 280: 40032-40
1424 Tamura Y, Endo T (2017) Role of Intra- and Inter-mitochondrial Membrane Contact
1425 Sites in Yeast Phospholipid Biogenesis. Advances in experimental medicine and biology
1426 997: 121-133
1427 Tan W, Colombini M (2007) VDAC closure increases calcium ion flux. Biochimica et
1428 biophysica acta 1768: 2510-5
1429 Tasseva G, Bai HD, Davidescu M, Haromy A, Michelakis E, Vance JE (2013)
1430 Phosphatidylethanolamine deficiency in Mammalian mitochondria impairs oxidative
1431 phosphorylation and alters mitochondrial morphology. The Journal of biological
1432 chemistry 288: 4158-73
1433 Tatsuta T, Scharwey M, Langer T (2014) Mitochondrial lipid trafficking. Trends in cell
1434 biology 24: 44-52
1435 Vance JE (1990) Phospholipid synthesis in a membrane fraction associated with
1436 mitochondria. The Journal of biological chemistry 265: 7248-56
1437 Vance JE (2014) MAM (mitochondria-associated membranes) in mammalian cells: lipids
1438 and beyond. Biochimica et biophysica acta 1841: 595-609
1439 Vance JE, Tasseva G (2013) Formation and function of phosphatidylserine and
1440 phosphatidylethanolamine in mammalian cells. Biochimica et biophysica acta 1831:
1441 543-54
1442 Wang H, Ma Q, Qi Y, Dong J, Du X, Rae J, Wang J, Wu WF, Brown AJ, Parton RG, Wu JW,
1443 Yang H (2019) ORP2 Delivers Cholesterol to the Plasma Membrane in Exchange for
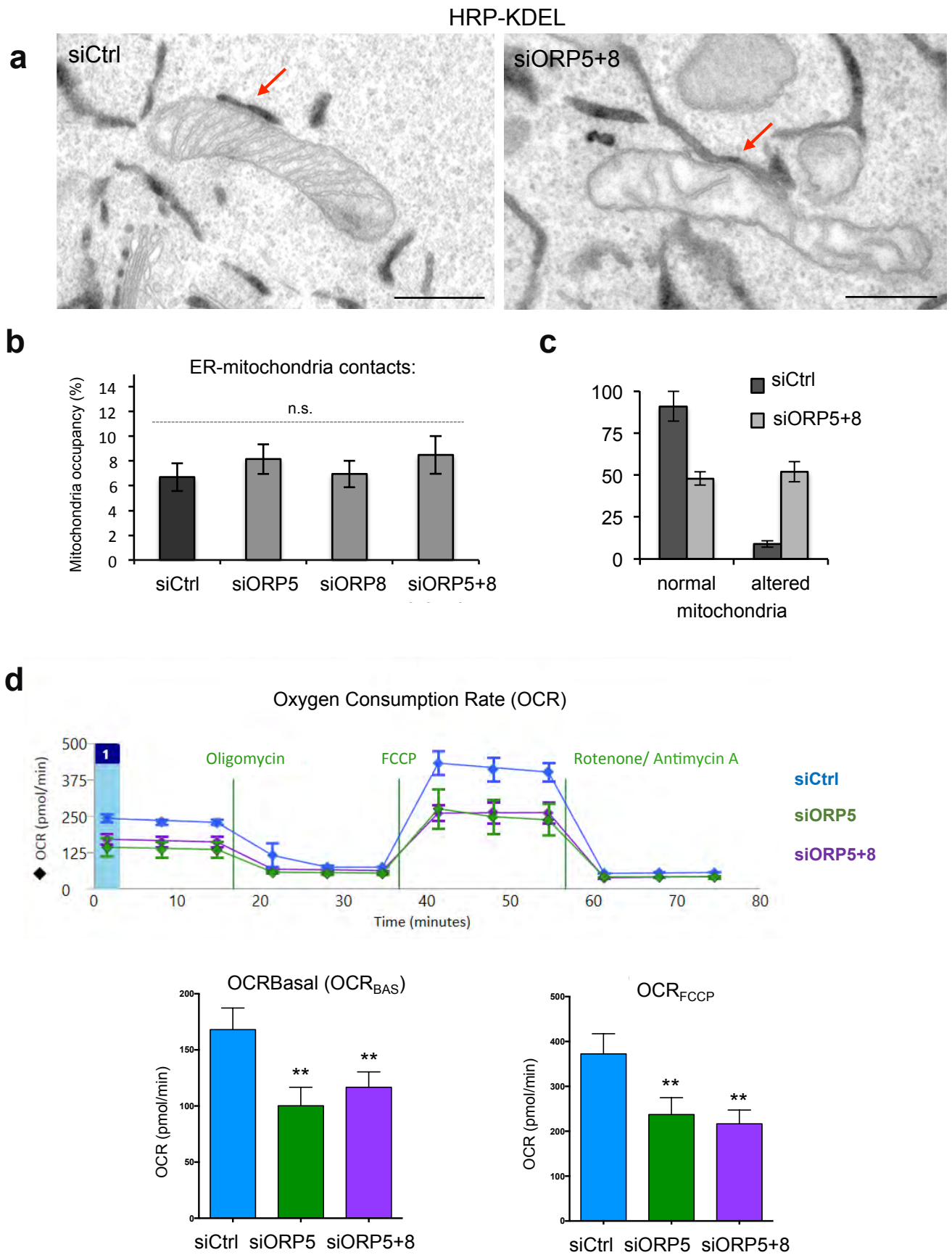1444 Phosphatidylinositol 4, 5-Bisphosphate (PI(4,5)P2). Mol Cell 73: 458-473 e7

1445   Wideman JG (2015) The ubiquitous and ancient ER membrane protein complex (EMC):
1446   tether or not? F1000Res 4: 624
1447   Wideman JG, Balacco DL, Fieblinger T, Richards TA (2018) PDZD8 is not the 'functional
1448   ortholog' of Mmm1, it is a paralog. F1000Res 7: 1088
1449   Wiel C, Lallet-Daher H, Gitenay D, Gras B, Le Calve B, Augert A, Ferrand M, Prevarskaya
1450   N, Simonnet H, Vindrieux D, Bernard D (2014) Endoplasmic reticulum calcium release
1451   through ITPR2 channels leads to mitochondrial calcium accumulation and senescence.
1452   Nature communications 5: 3792
1453   Wollweber F, von der Malsburg K, van der Laan M (2017) Mitochondrial contact site and
1454   cristae organizing system: A central player in membrane shaping and crosstalk.
1455   Biochimica et biophysica acta 1864: 1481-1489
1456

a

Streptavidin-coated bead

Donor liposomes
Biotinylated,
TopFluor-labeled

Acceptor
liposomes

Fluorescent
lipid transfert

+/- ORP5/8 ORD

b

Lipid transfer (%)

* *

+ORD8 +ORD8 +ORD8
PS   **PC**   **PE**

Lipid transfer (%)

* *

+ORD5 +ORD5 +ORD5
PS   **PC**   **PE**

c

siCtrl   siORP5   siORP8

TC Crude Mito Mito MAM   TC Crude Mito Mito MAM   TC Crude Mito Mito MAM

IP3R-3
ORP5
ORP8
Cyt C

d

Lipidomic analysis of PE content:

Total PE (nmol/mg protein)

*

siCtrl   siORP5   siORP8   siCtrl   siORP5   siORP8
Mito   Mito   Mito   Cell   Cell   Cell

e

PS-to-PE conversion :

PE:PS ratio

*

* *

siCtrl   siORP5   siORP8   siORP5 + siORP8

f

PS-to-PE conversion:

I=β-Chl-L-ala

**   n.s.

n.s.

siCtrl -I   siCtrl +I   siORP5 -I   siORP5 +I

g

siCtrl siORP5 siORP8 siORP5+8

ORP5
ORP8
PISD
Actin

siCtrl siORP5 siORP8 siORP5+8

ORP5
ORP8
PSS1
Actin

h

mito

PS

PE   PS

ORP5/8   ER

Figure 1

Figure 1. ORP5 and ORP8 mediate PS transfer *in vitro* and at ER-mitochondria contact sites

(a) Schematic cartoon showing the *in vitro* assay used to study ORP5/8 ORD-mediated lipid transport between liposomes. (b) Donor liposomes containing fluorescent lipids (97 mol% POPC, 1 mol% TopFluor-PS, -PC or -PE and 2 mol% of biotinylated-PE) and pre-bound to streptavidin beads were mixed at a 1:1 molar ratio with acceptor liposomes (100 mol% POPC) in the presence or absence of ORP5 or ORP8 ORD domains (250 µM of donor and acceptor liposomes and 0,3 µM of proteins in the reaction solution). The increase in fluorescence in the acceptor liposomes, which remain unbound in the solution, was measured after 1 hour of incubation at 37°C. Data are presented as % of transferred lipid ±SEM and are the mean of six independent experiments. **$P<0,001$ (c) Crude mitochondria, mitochondria, and MAM fractions were purified from Ctrl, ORP5 and ORP8 siRNA-treated HeLa cells. Equal amounts of protein from each fraction were loaded on a 4–20% gradient SDS–PAGE gel and immunoblotted using anti-ORP5, anti-ORP8, anti-IP3R-3 (MAM protein), and anti-cytochrome c (mitochondrial protein). Mito, mitochondria; MAM, mitochondria-associated ER membrane. (d) Mass spectrometry (MS)-based quantification of the PE content (nmol/mg protein) of mitochondria isolated from Ctrl, ORP5 or ORP8 knockdown cells and of Ctrl, ORP5 or ORP8 knockdown intact cells. Data are shown as mean of three independent replicates ±SEM. *$P<0,05$. (e-f) HeLa cells transfected with siCtrl, siORP5, siORP8 or siORP5+ORP8 RNAi oligos were incubated with L-[^{3}H(G)]serine (30.9 Ci/mmol) for 18 hours (e). After extraction and separation of lipids by TLC, PS and PE spots were scraped and analyzed for [^{3}H] radioactivity, as described under "Methods". Each condition was analyzed in triplicate in each of three independent biological replicates. Data are presented as mean of PE:PS ratio ±SEM. *$P<0,05$, **$P<0,01$ compared to Ctrl. (f) Cells transfected with siCtrl and siORP5 oligos were treated with b-Chloro-L-alanine (b-Chl-L-ala, inhibitor of Ser-palmitoyltransferase) or untreated, then pulsed with 15 µCi/ml of [^{3}H(G)]serine for 1 hour and chased for 12 hours in serum-free DMEM, before analysis. n.s. not significant, **$P<0,01$ compared to Ctrl. (g) WB analysis showing ORP5, ORP8, PSD1, PSS1 and Actin levels in protein lysates from HeLa cells treated with either Ctrl siRNAs or with siRNAs against ORP5 or/and ORP8. (h) Schematic representation of non-vesicular PS transfer mediated by ORP5/8 at ER-mitochondria contact sites. PS is transported to mitochondrial membranes where it is rapidly converted into mitochondrial PE.

HRP-KDEL

a siCtrl | siORP5+8

b ER-mitochondria contacts:

Mitochondria occupancy (%)

n.s.

siCtrl | siORP5 | siORP8 | siORP5+8

c

■ siCtrl
□ siORP5+8

normal | altered
mitochondria

d Oxygen Consumption Rate (OCR)

OCR (pmol/min)

Oligomycin | FCCP | Rotenone/ Antimycin A

siCtrl
siORP5
siORP5+8

Time (minutes)

OCRBasal (OCR$_{BAS}$)

OCR (pmol/min)

** | **

siCtrl | siORP5 | siORP5+8

OCR$_{FCCP}$

OCR (pmol/min)

** | **

siCtrl | siORP5 | siORP5+8

Figure 2

Figure 2. ORP5 and ORP8 knockdown affect mitochondria morphology and respiratory function but not the aboundance of ER-mitochondria contact sites

(a) Electron micrographs of HRP-KDEL-expressing HeLa cells treated with Ctrl siRNAs (siCtrl) or siRNAs against ORP5 and ORP8 (siORP5+siORP8). Red arrows indicate ER-mitochondria contact sites. Scale bar, 500 nm. (b) Quantifications of the extent of ER-mitochondria contact sites in siCtrl, siORP5, siORP8 and siORP5+8 cells expressing HRP-KDEL. Data are shown as % of the ER in contact with mitochondria (mitochondria occupancy) ±SEM, n = 20 cell profiles and ±900 mitochondria; n.s; not significant. (c) Quantifications of the number of mitochondria with aberrant cristae morphology in the indicated siRNA conditions. Data are shown as % of mitochondria ±SEM, n = 20 cell profiles and ±700 mitochondria. **P<0,01 compared to siCtrl. (d) Mitochondrial oxygen consumption rate (OCR) measured in Ctrl, ORP5 or ORP8, and ORP5+8 siRNA-treated HeLa cells. OCR trace was obtained by sequential measurement of basal OCR (OCR_{BAS}), OCR after the addition of Oligomycin, OCR after the addition of FCCP (OCR_{FCCP}) and OCR after the addition of Rotenone/Antimycin A. Note the reduced OCR in siORP5 and siORP5+8 cells compared to Ctrl siRNA cells. Error bars denote ±SEM. Data shown in the bar charts are the mean of 4 independent repeats (n=4). **P<0,01 compared to Ctrl.
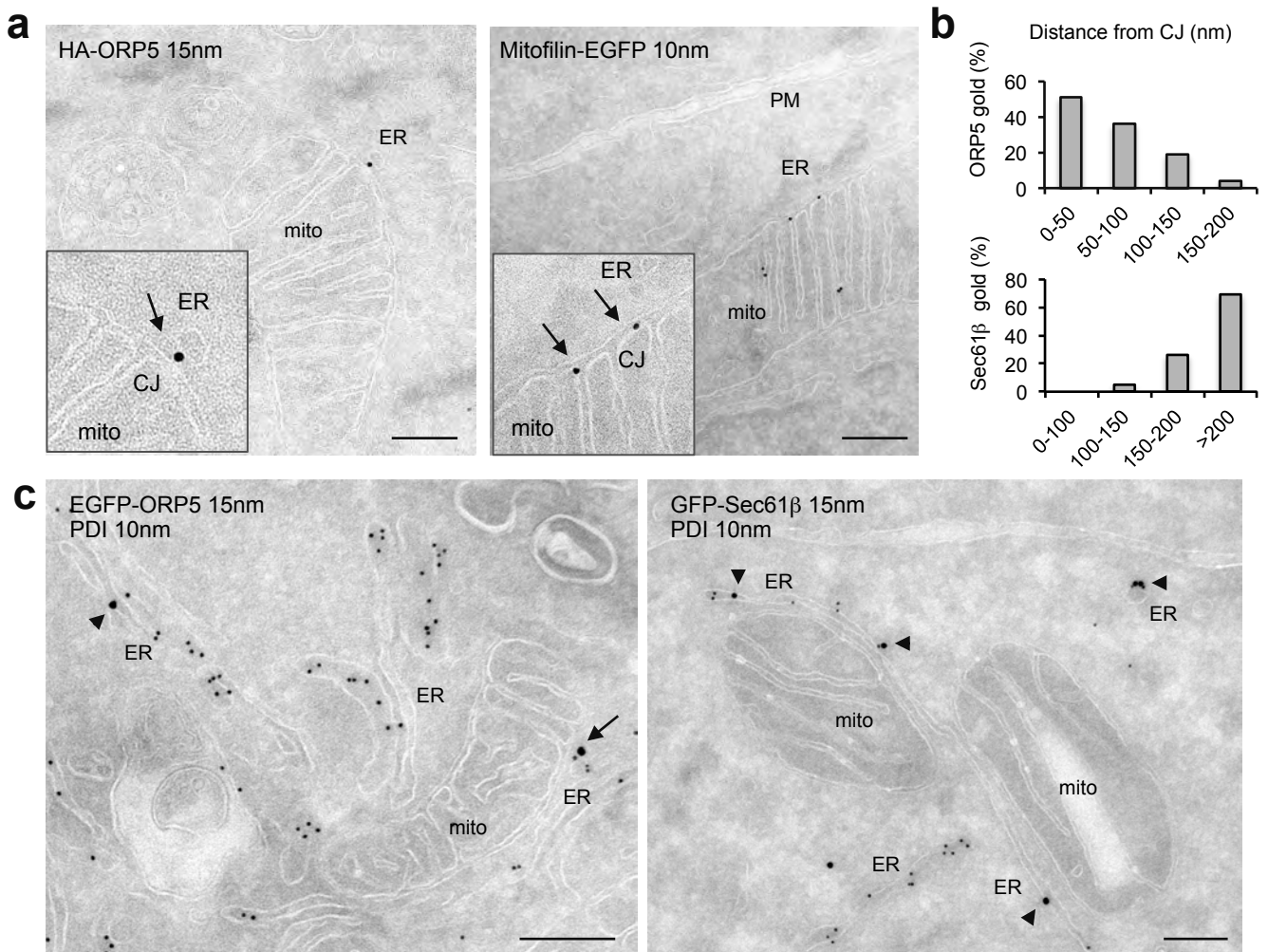
Figure 3. ORP5 localize at ER-mitochondria contact sites near cristae junctions (CJ)

(a) Electron micrographs of ultrathin cryosections of HeLa cells transfected with HA-ORP5 or Mitofilin-EGFP and immunogold stained with anti-HA or anti-GFP (10 or 15 nm gold), showing ORP5 localization at ER-mitochondria contacts in close proximity to CJ (arrow) and the localization of the MICOS complex (Mitofilin) at CJ (arrows). Scale bar 250 nm. (b) Quantification of the proximity of HA-ORP5 and EGFP-Sec61β gold particles to the CJ. Results are presented as the percentage of ORP5 or Sec61β gold particles (n = 23 cell profiles) at specific ranges of distance (in nm) from CJ. (c) Electron micrographs of ultrathin cryosections of HeLa cells transfected with EGFP-ORP5 or GFP-Sec61β and immunogold labeled with anti-GFP (15 nm gold) and anti-PDI (10nm gold). Note ORP5 localization at ER-mitochondria contacts near CJ (arrow) and Sec61β localization to ER membranes not in contact with the mitochondria membranes (arrowheads). Scale bar 250 nm.

Figure 3

a

Mass-Spectrometry Analysis

Protein	Localization	IP EGFP	IP EGFP-ORP5	IP EGFP-ORP5ΔPH
			Mascot Score	
ORP5	MAMs	0	9689	12192
ORP8	MAMs	31	930	690
Mitofilin	IMM	43	579	1150
SAM50	OMM	0	237	516
Metaxin2	OMM	0	32	175
RHOT2	OMM	0	131	119
TOM22	OMM	0	77	95
PTPIP51	OMM	0	76	73

b

c

d

e
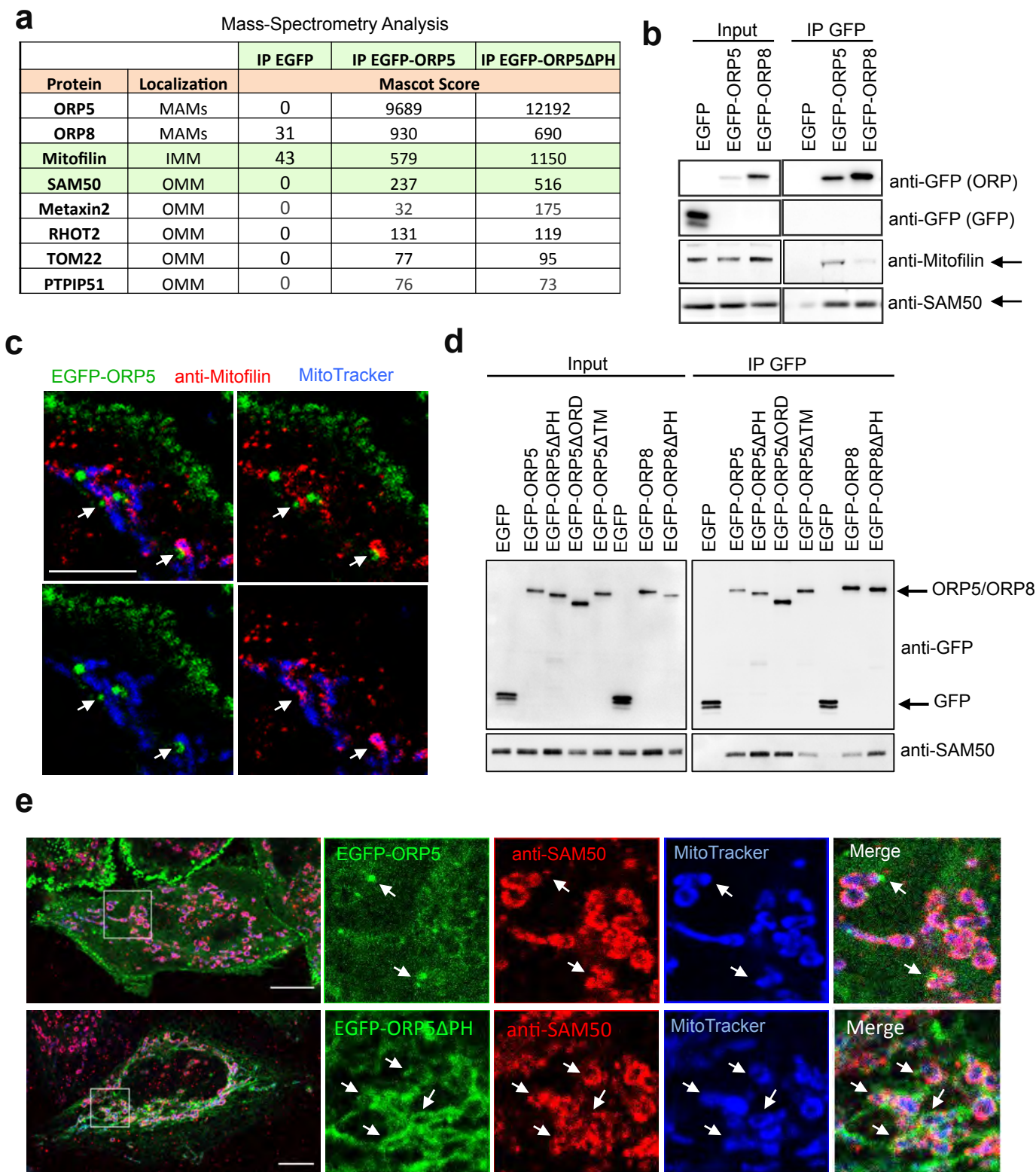
Figure 4

Figure 4. ORP5 and ORP8 interact with the MIB/MICOS complex at ER-mitochondria contacts near CJ

(a) Identification of mitochondrial proteins associated to mitochondrial outer or inner membranes (OMM, IMM) that interact with EGFP-tagged ORP5 constructs by mass spectrometry. Note the presence of some proteins of the MIB complex: Mitofilin, SAM50 and Metaxin2. Interaction scores (Mascot scores) of Mitofilin, SAM50 and Metaxin2 with the EGFP-ORP5ΔPH construct are stronger than with EGFP-ORP5. (b) EGFP-ORP5, EGFP-ORP8 or EGFP alone were transfected in HeLa cells then immuno-precipitated from lysates and analyzed by western blot using antibodies against GFP (for ORP5 or ORP8), Mitofilin or SAM50. (c) Confocal images of a region of HeLa cells transfected with EGFP-ORP5 (green) and stained with MitoTracker (blue) and anti-Mitofilin (red) antibody. Arrows point to ORP5-positive ER elements in proximity to mitofilin-enriched microdomains on mitochondria. Scale bar, 5 µm. (d) EGFP-ORP5, EGFP-ORP5ΔPH, EGFP-ORP5ΔORD, EGFP-ORP5ΔTM, EGFP-ORP8, EGFP-ORP8ΔPH or EGFP alone were transfected in HeLa cells then immuno-precipitated from lysates and analyzed by western blot using antibodies against GFP (for ORP5 or ORP8) or against SAM50. (e) Confocal images of HeLa cells transfected with either EGFP-ORP5 or EGFP-ORP5ΔPH (green) and stained with MitoTracker (Blue) and anti-SAM50 (red) antibody. Arrows point to ORP5-positive ER elements in proximity to SAM50-positive mitochondria. Insets show magnifications of the boxed regions. Scale bar, 10 µm.

a

b

Radiometric measurement of newly synthetised PE

c

d

ER-mitochondria contacts
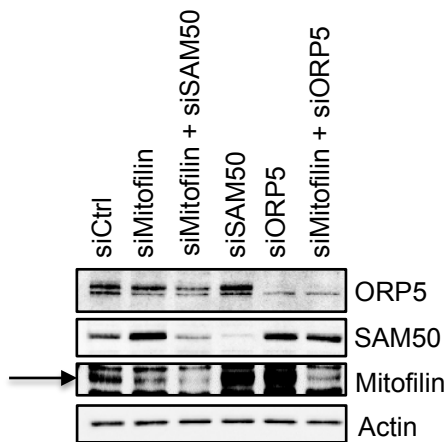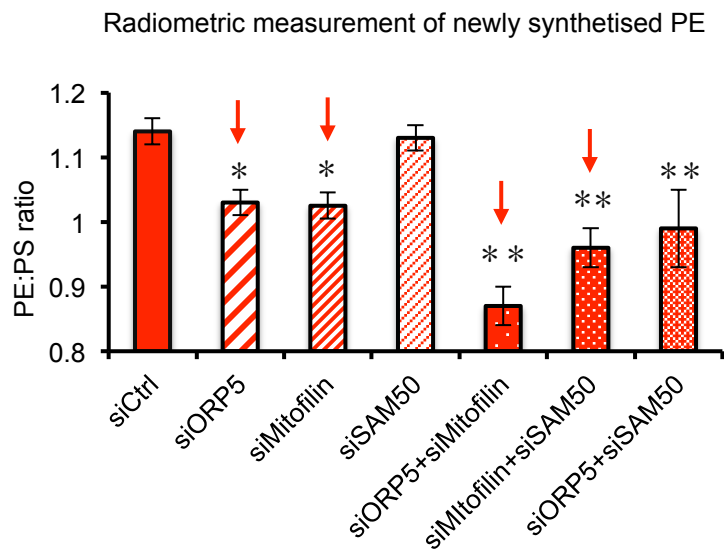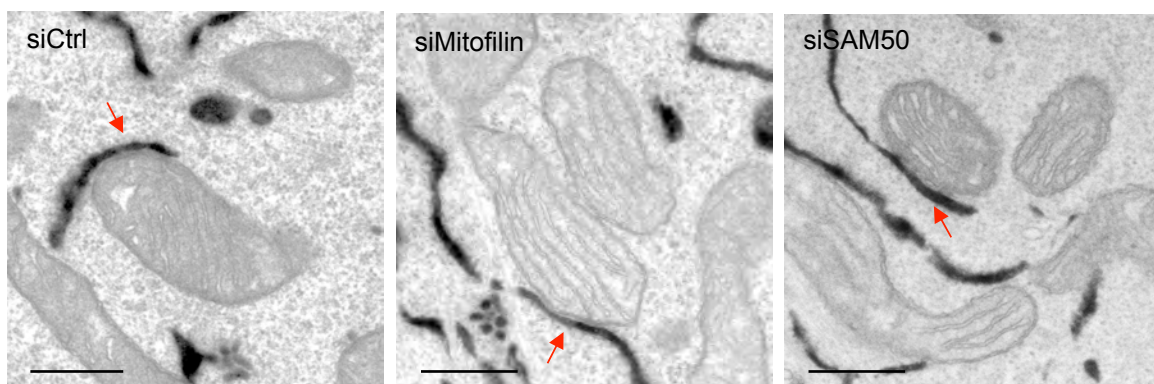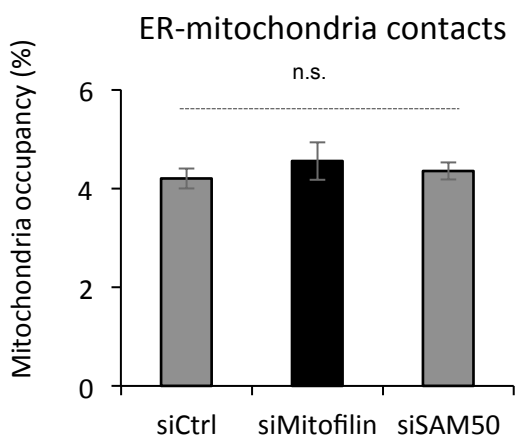
Figure 5

Figure 5. ORP5 and the MIB/MICOS complex cooperate to mediate non-vesicular transport of PS from the ER to mitochondrial membranes
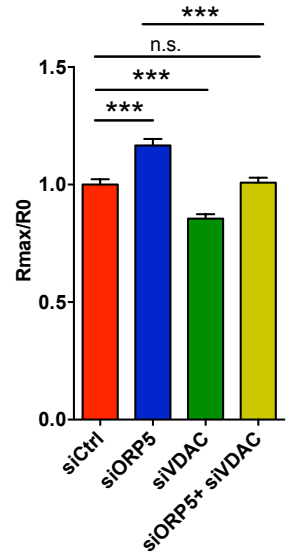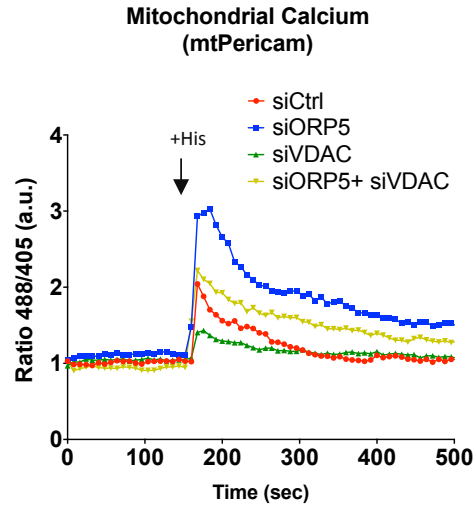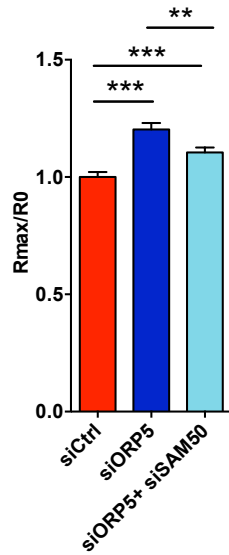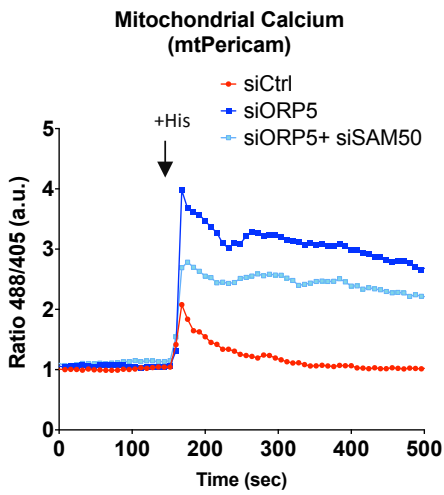
(a) Western analysis showing ORP5, SAM50, Mitofilin and Actin levels in protein lysates from HeLa cells treated with siRNA against Ctrl, ORP5, Mitofilin or SAM50. Arrow indicates the specific band for Mitofilin. (b) Radiometric measurement of PS-to-PE conversion in the indicated siRNAs. Data are presented as mean of PE:PS ratio ±SEM. Each condition was performed in triplicate in each of the independent biological replicates (n = 5 for siCtrl and siORP5; n = 4 for siSAM50; n = 3 for the other siRNAs conditions). *P<0,05, **P<0,01 compared to Ctrl. (c) Representative electron micrographs of HeLa cells treated with Ctrl siRNAs or siRNAs against Mitofilin or SAM50 and transfected with HRP-KDEL. Red arrows indicate ER-mitochondria contact sites. Scale bar, 500 nm. (d) Quantifications of the extent of ER-mitochondria contact sites in Ctrl, Mitofilin and SAM50 knockdown cells expressing HRP-KDEL. Data are shown as % of the ER in contact with mitochondria (mitochondria occupancy) ±SEM, n = 30 for siCtrl, n = 20 cell profiles for siMitofilin and siSAM50 and 1 000 mitochondria; n.s; not significant.
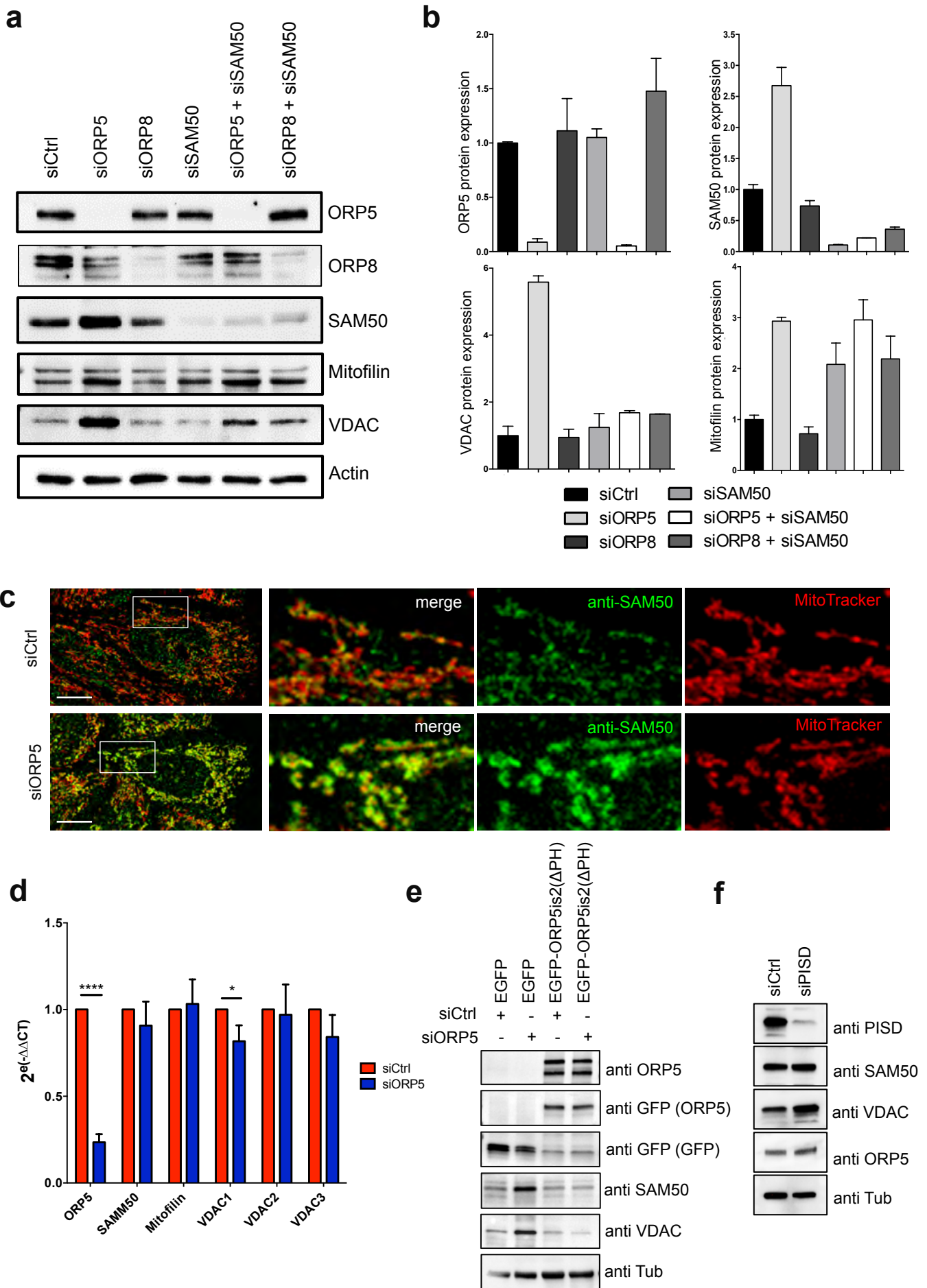
Figure 6

Figure 6. Silencing of ORP5 but not ORP8 specifically increases VDAC protein level in a SAM50-dependent manner

(a) Western analysis showing ORP5, ORP8, SAM50, Mitofilin, VDAC and Actin levels in protein lysates from HeLa cells treated with either Ctrl siRNAs, or with siRNAs against ORP5, ORP8, or SAM50. (b) Quantification of ORP5, SAM50, VDAC and Mitofilin protein expression in the indicated knockdown conditions. Normalized data are shown as mean ±SEM (n = 3). (c) Confocal images of Ctrl and ORP5 knockdown HeLa cells labeled with MitoTracker (red) and immunostained using anti-SAM50 antibody (green). Scale bar, 10 μm. (d) Quantitative RT-PCR analysis of ORP5, SAM50, Mitofilin, VDAC1, VDAC2 and VDAC3 in ORP5 knockdown cells versus control HeLa cells. y axis: $2^{(-\Delta\Delta Ct)}$ value represents differences between the mean Ct (Cycle threshold) values of tested genes and those of reference gene (SDHA). (e) HeLa cells treated with siRNA against Ctrl and ORP5, were transfected with EGFP alone or with EGFP-ORP5is2 (ORP5 isoform 2) and cell lysates following SDS-PAGE were immunoblotted with antibodies against GFP (to detect EGFP and EGFP-ORP5), ORP5, SAM50, VDAC and Tubulin. Note the rescue of SAM50 and VDAC levels in siORP5 cells transfected with EGFP-ORP5is2 as compared to cells expressing EGFP alone. (f) Western analysis showing PISD, SAM50, VDAC, ORP5 and Tubulin levels in protein lysates from HeLa cells treated with either Ctrl siRNAs, or with siRNAs against PISD.
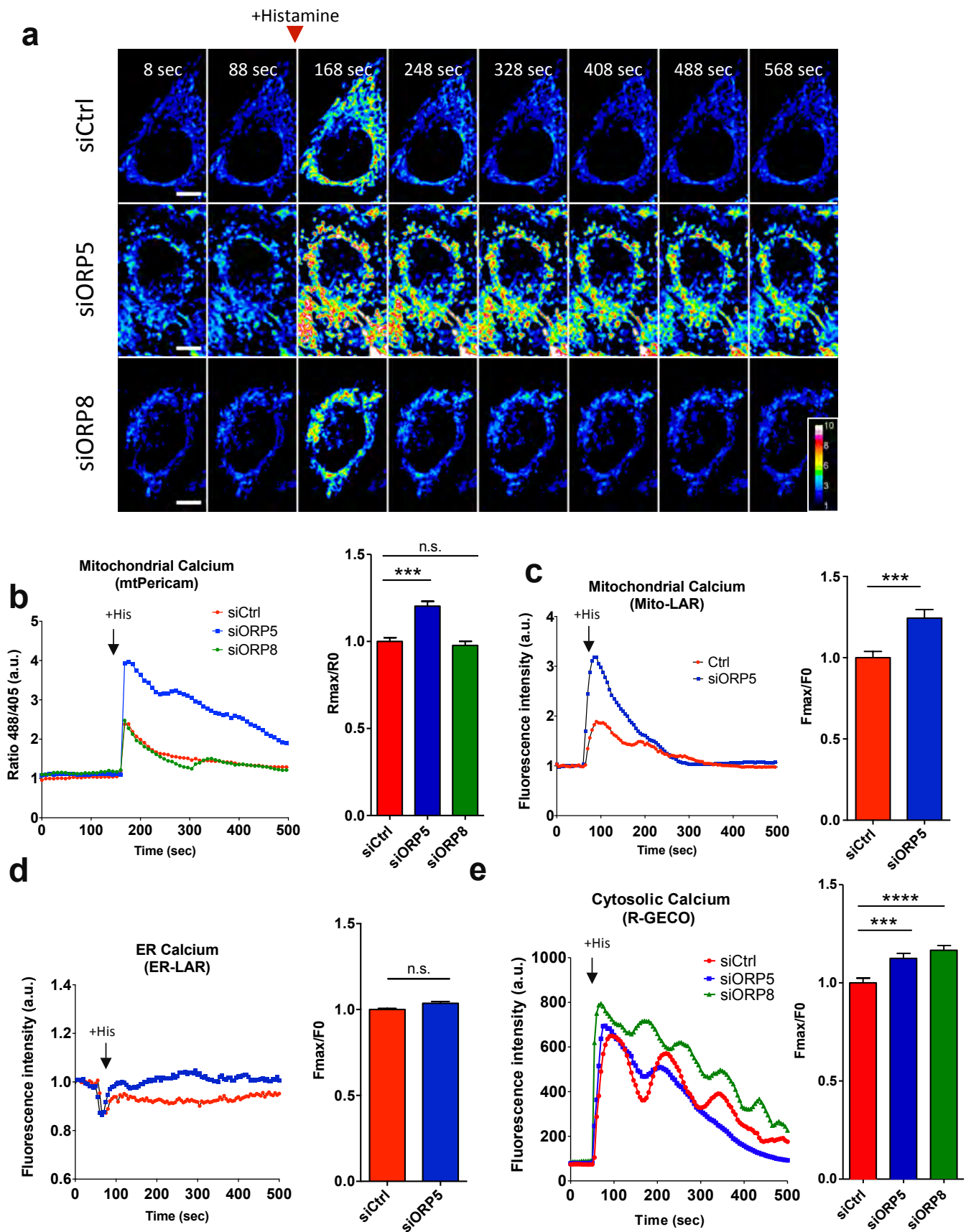
Figure 7

Figure 7. Silencing of ORP5 but not ORP8 increases mitochondrial calcium

(a) Pseudocolor 488/405 ratio time-lapse images of a representative Ctrl, ORP5 or ORP8 knockdown HeLa cell expressing mt-Pericam before and after histamine treatment. Scale bar 10 μm. (b) Representative curves of Ctrl, ORP5 and ORP8 knockdown HeLa cells expressing mt-Pericam showing the ratio of Pericam fluorescence before and after histamine treatment (+His). The change in the ratio of Pericam fluorescence after histamine treatment under each condition was compared (Rmax/R0). Data are presented as normalized mean ±SEM, n = 3 per condition, ***, p< 0.001; n.s; not significant. (c) Representative curves of Ctrl and ORP5 knockdown HeLa cells expressing the GECO construct Mito-LAR showing the fluorescence before and after histamine treatment. The change in fluorescence after histamine treatment under each condition was compared (Fmax/F0). Data are presented as normalized mean ±SEM, n = 3 per condition, ***, p< 0.001; n.s; not significant. (d) Representative curves of Ctrl and ORP5 knockdown HeLa cells expressing the GECO construct ER-LAR showing the fluorescence before and after histamine treatment. The change in fluorescence after histamine treatment under each condition was compared (Fmax/F0). Data are presented as normalized mean ±SEM, n = 3 per condition, n.s; not significant. (e) Representative curves of Ctrl, ORP5 and ORP8 knockdown HeLa cells expressing the GECO construct R-GECO showing the fluorescence before and after histamine treatment. The change in fluorescence after histamine treatment under each condition was compared (Fmax/F0). Data are presented as normalized mean ±SEM, n = 3 per condition, ***, p< 0.001 and ****, p< 0.0001; n.s; not significant.

a

siCtrl siORP5 siVDAC siORP5 + siVDAC

ORP5
VDAC
Actin

b

**Mitochondrial Calcium
(mtPericam)**

- siCtrl
- siORP5
- siVDAC
- siORP5+ siVDAC

+His

Ratio 488/405 (a.u.)

Time (sec)

Rmax/R0

***
n.s.
***
***

siCtrl
siORP5
siVDAC
siORP5+ siVDAC

c

**Mitochondrial Calcium
(mtPericam)**

- siCtrl
- siORP5
- siORP5+ siSAM50

+His

Ratio 488/405 (a.u.)

Time (sec)

Rmax/R0

**
***
***

siCtrl
siORP5
siORP5+ siSAM50
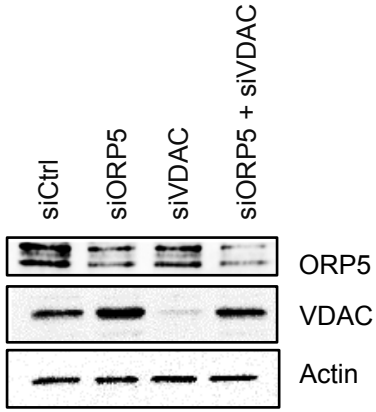
Figure 8

Figure 8. Calcium increase induced by ORP5 knockdown is dependent on SAM50 and VDAC

(a) Western analysis showing ORP5 and VDAC protein levels in Ctrl, ORP5 and VDAC siRNA-treated HeLa cells. (b). Representative curves of Ctrl, ORP5, VDAC and ORP5+VDAC knockdown HeLa cells expressing mt-Pericam showing the ratio of Pericam fluorescence before and after histamine treatment (+His). The change in the ratio of Pericam fluorescence after histamine treatment under each condition was compared (Rmax/R0). Data are presented as normalized mean ±SEM, n = 3 per condition, ***, p< 0.001; n.s; not significant.   (c). Representative curves of Ctrl, ORP5 and ORP5+SAM50 knockdown HeLa cells expressing mt-Pericam showing the ratio of Pericam fluorescence before and after histamine treatment (+His). The change in the ratio of Pericam fluorescence after histamine treatment under each condition was compared (Rmax/R0). Data are presented as normalized mean ±SEM, n = 3 per condition, ***, p< 0.001; n.s; not significant.
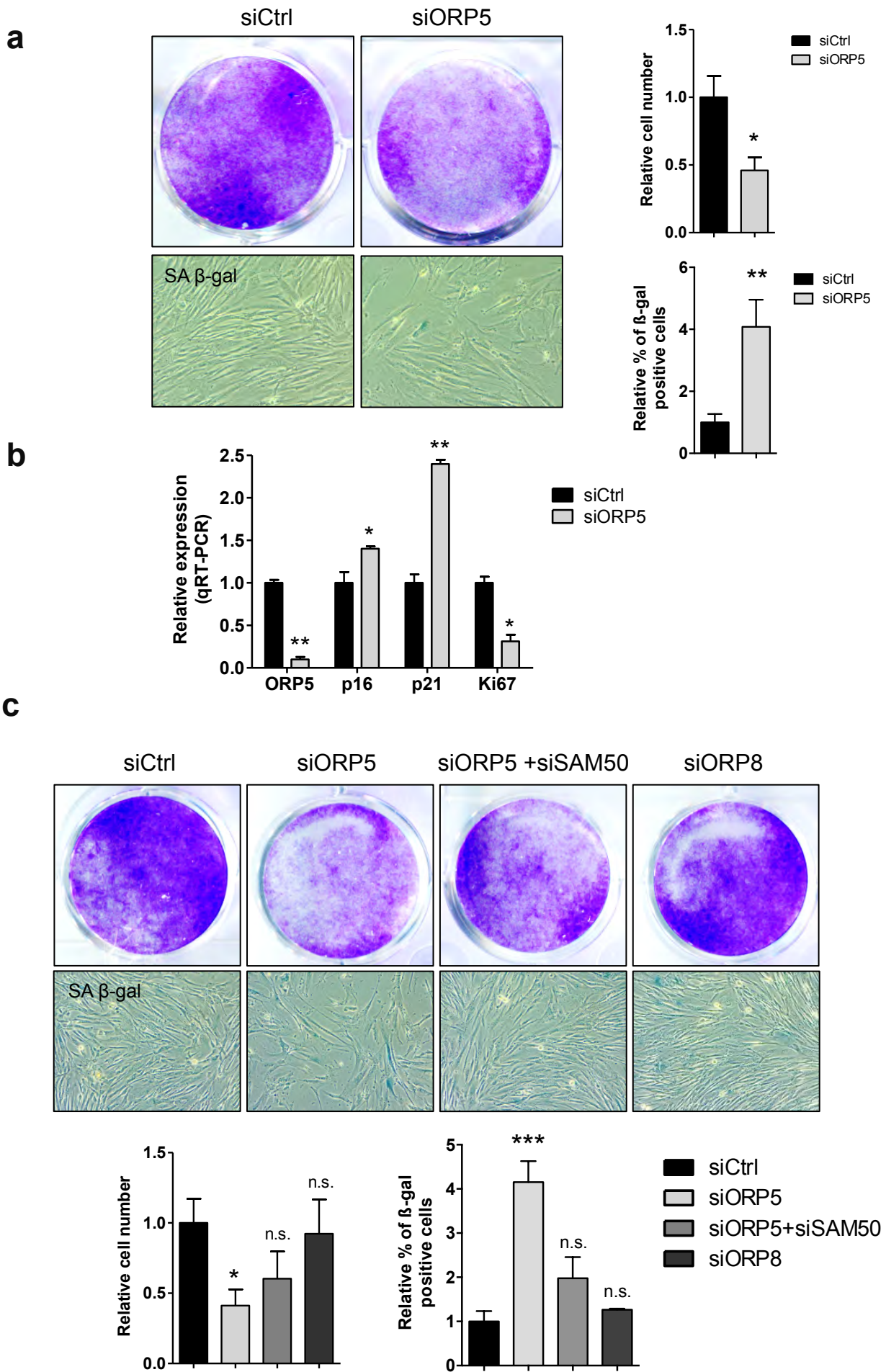
Figure 9

Figure 9. Cell senescence promoted by ORP5 knockdown is dependent on SAM50

 (a) MCR5 cells transfected with control siRNA or with siRNA against ORP5 were fixed and then stained with crystal violet solution (CA) or with SA-β-galactosidase (SA-β-Gal) staining solution. The graph on the top right shows the relative cell number determined by crystal violet staining. The graph on the bottom right shows the relative percentage of β-gal positive cells determined by SA-β-galactosidase assay. Data are presented as normalized mean ±SEM, n = 3 per condition, **, $p < 0.01$; *, $p < 0.05$. (b) Quantitative RT-PCR analysis of ORP5, p16, p21 and Ki67 in ORP5 knockdown cells and control HeLa cells. y axis:$2^{(-\Delta\Delta Ct)}$ value represents differences between the mean Ct (Cycle threshold) values of tested genes and those of reference genes (PGK1 and HPRT1). Data are presented as normalized mean ±SEM, n = 3 per condition, **, $p < 0.01$; *, $p < 0.05$. (c) MCR5 cells transfected with control siRNA or with siRNA against ORP5, SAM50 or ORP8 were fixed and then stained with crystal violet solution or with SA-β-Gal staining solution. The graph on the left shows the relative cell number determined by crystal violet staining. The graph on the right shows the relative percentage of β-gal positive cells determined by SA-β-galactosidase assay. Data are presented as normalized mean ±SEM, n = 3 per condition, ***, $p < 0.001$; *, $p < 0.05$; n.s; not significant.

Model:
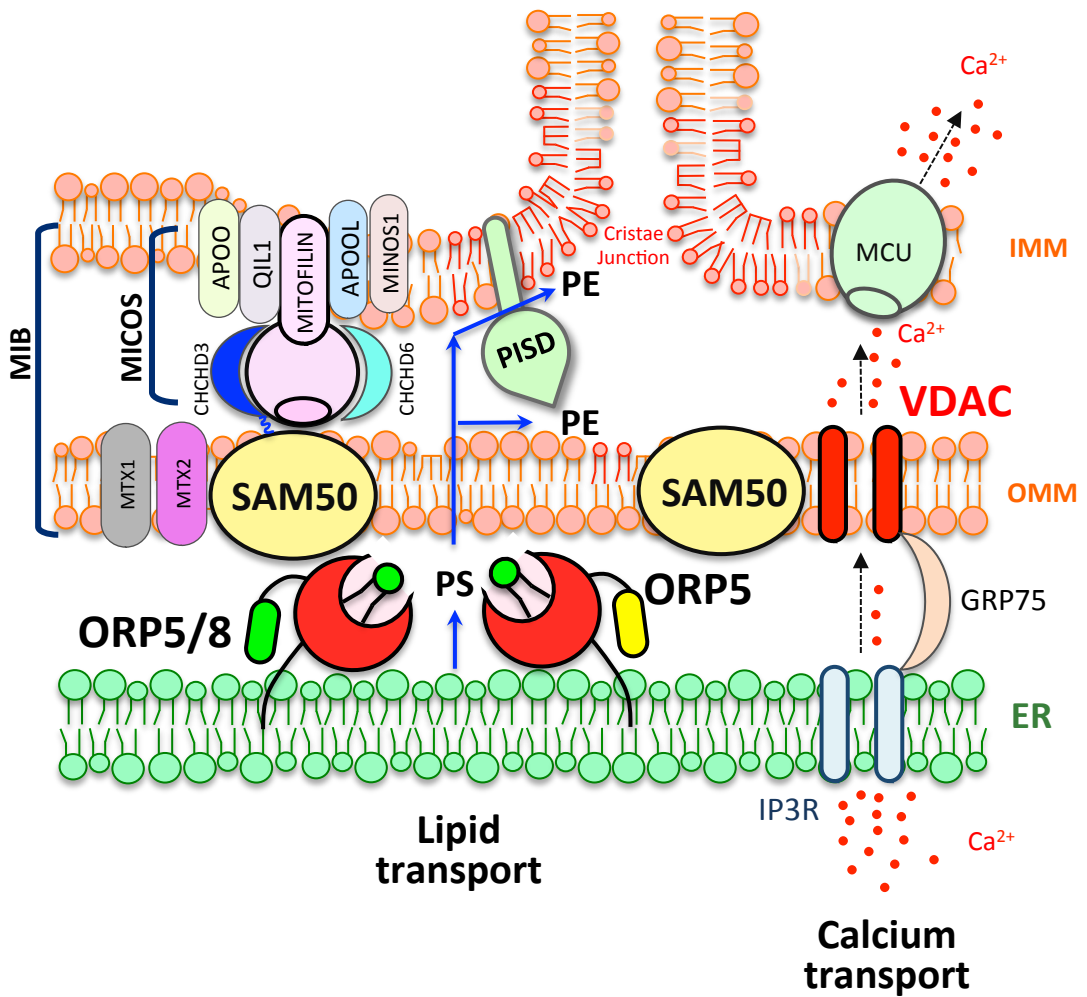
Figure 10. Lipid and calcium transport occur at the same ER-mitochondria contact site microdomains and are regulated by a ORP5-SAM50-VDAC pathway

ORP5/8 are directly involved in the transfer of PS from ER to mitochondria at ER-mitochondria membrane contact sites. This transfer occurs at the level of cristae junctions (CJ) where ORP5/8 localize and interacts with the proteins of the MIB complex SAM50 and Mitofilin. This interaction facilitates the transfer of PS from ER to the mitochondrial membranes at the level of CJ and PS conversion into PE, a phospholipid that plays a critical role in cristae organization and mitochondrial function. ORP5 is also involved in calcium homeostasis by regulating the level of VDAC *via* modulation of SAM50 protein levels.

Figure 10
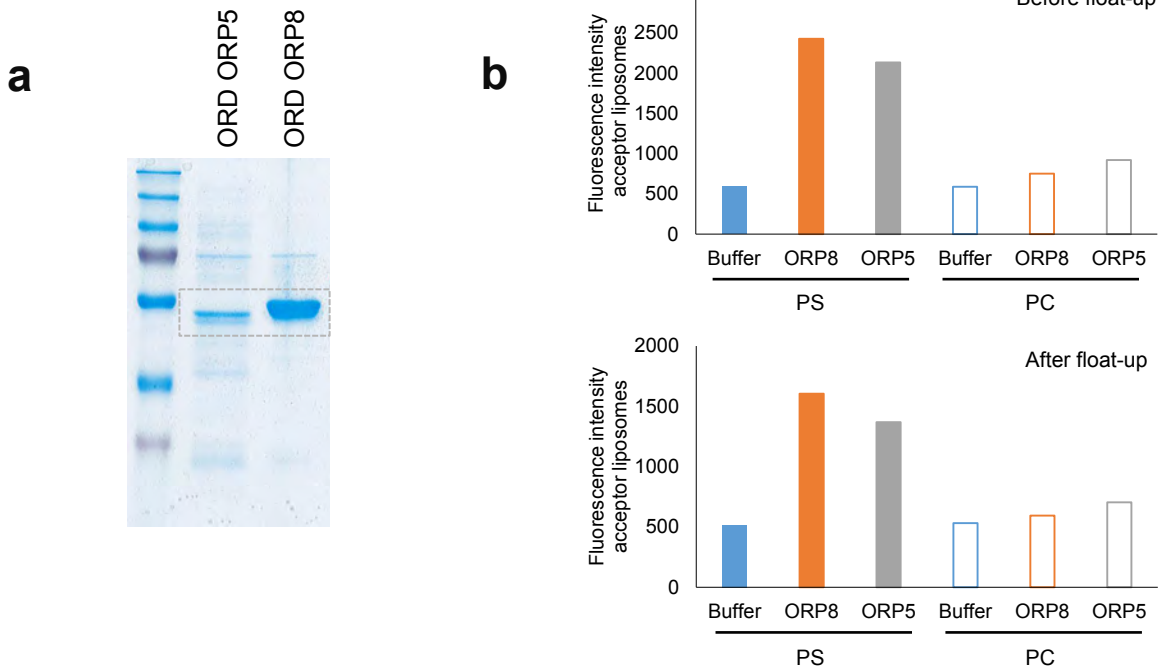
Figure S1. (a) Coomassie stained SDS-PAGE of the recombinant ORD domain of ORP5/8 proteins purified in BL21DE3 RILP cells. (b) Results of a lipid transfer experiment performed as in Fig. 1 a, b and presented as the fluorescence intensity of acceptor liposomes before (top panel) or after (bottom panel) their floatation on a Nycodenz gradient to confirm that fluorescence comes from the liposomes membrane.
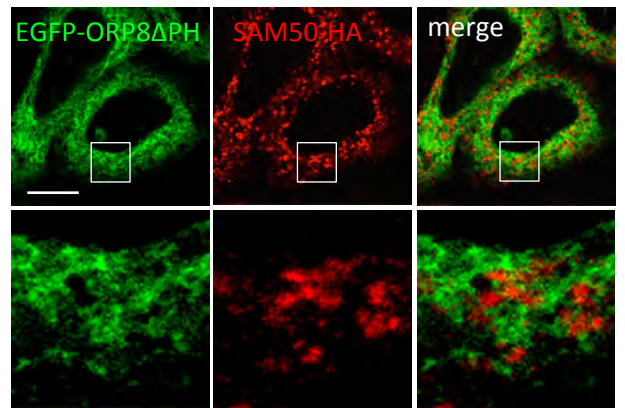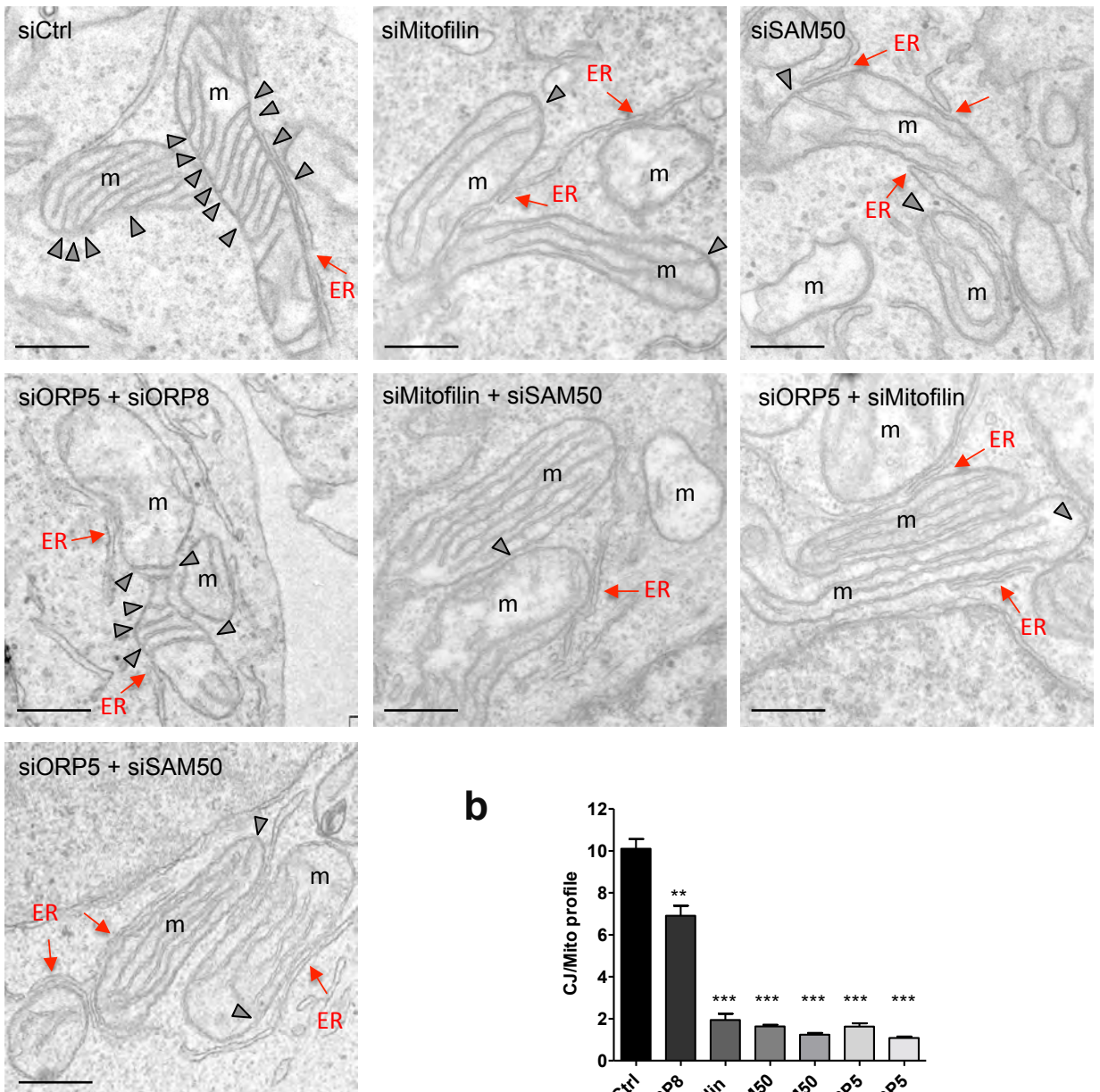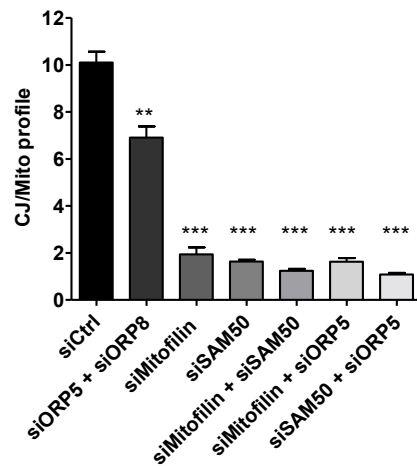
Figure S1
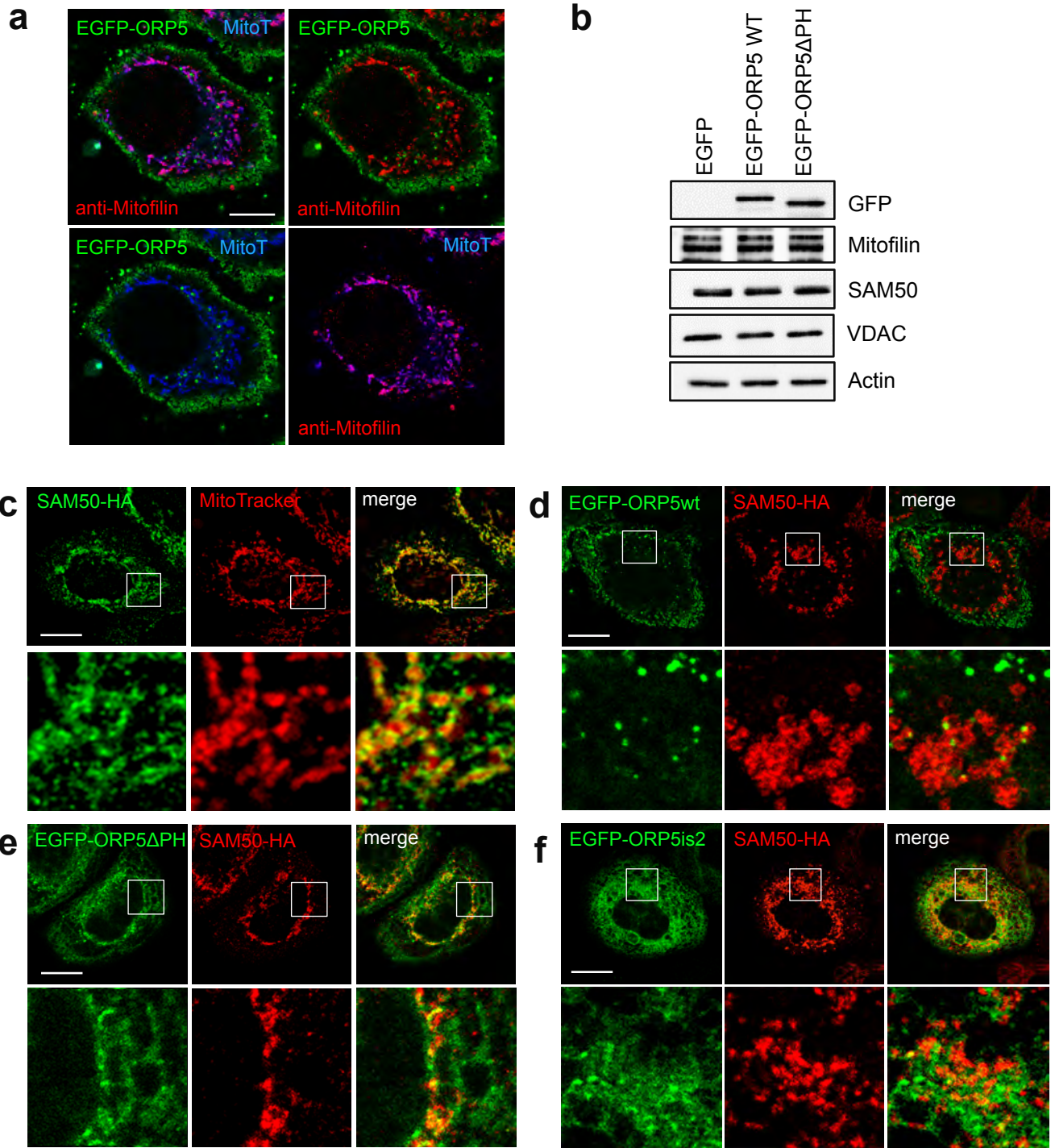
Figure S2

Figure S2. (a) Confocal micrograph of a HeLa cell (corresponding to boxed region in Fig 4c) transfected with EGFP-ORP5 (green) and stained with MitoTracker (blue) and anti-Mitofilin (red) antibody. Scale bar, 10 μm. (b) WB analysis showing GFP (EGFP-tagged constructs), Mitofilin, VDAC and SAM50 and Actin levels in protein lysates from HeLa cells transfected with either EGF construct (Control) or with EGFP-ORP5 or EGFP-ORP5ΔPH constructs. (c) Confocal images of a HeLa cell transfected with SAM50-HA and stained with HA antibody to detect SAM50 (green) and MitoTracker to label mitochondria (red). Insets show magnifications of the boxed regions. Scale bar, 10 μm. (d-f) Confocal images of HeLa cells transfected with EGFP-ORP5, EGFP-ORP5ΔPH or EGFP-ORP5is2 (green) together with SAM50-HA and stained with HA antibody to detect SAM50 (red). Insets show magnifications of the boxed regions. Scale bar, 10 μm.
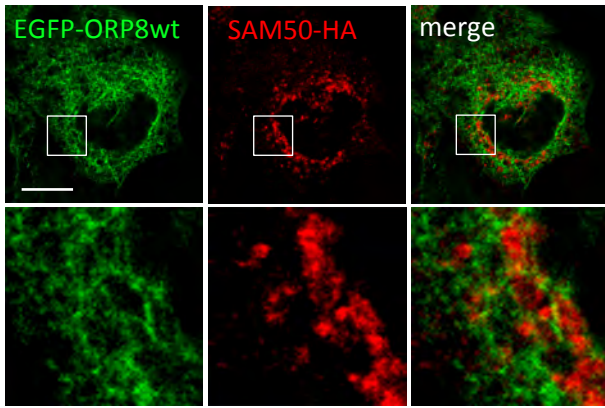
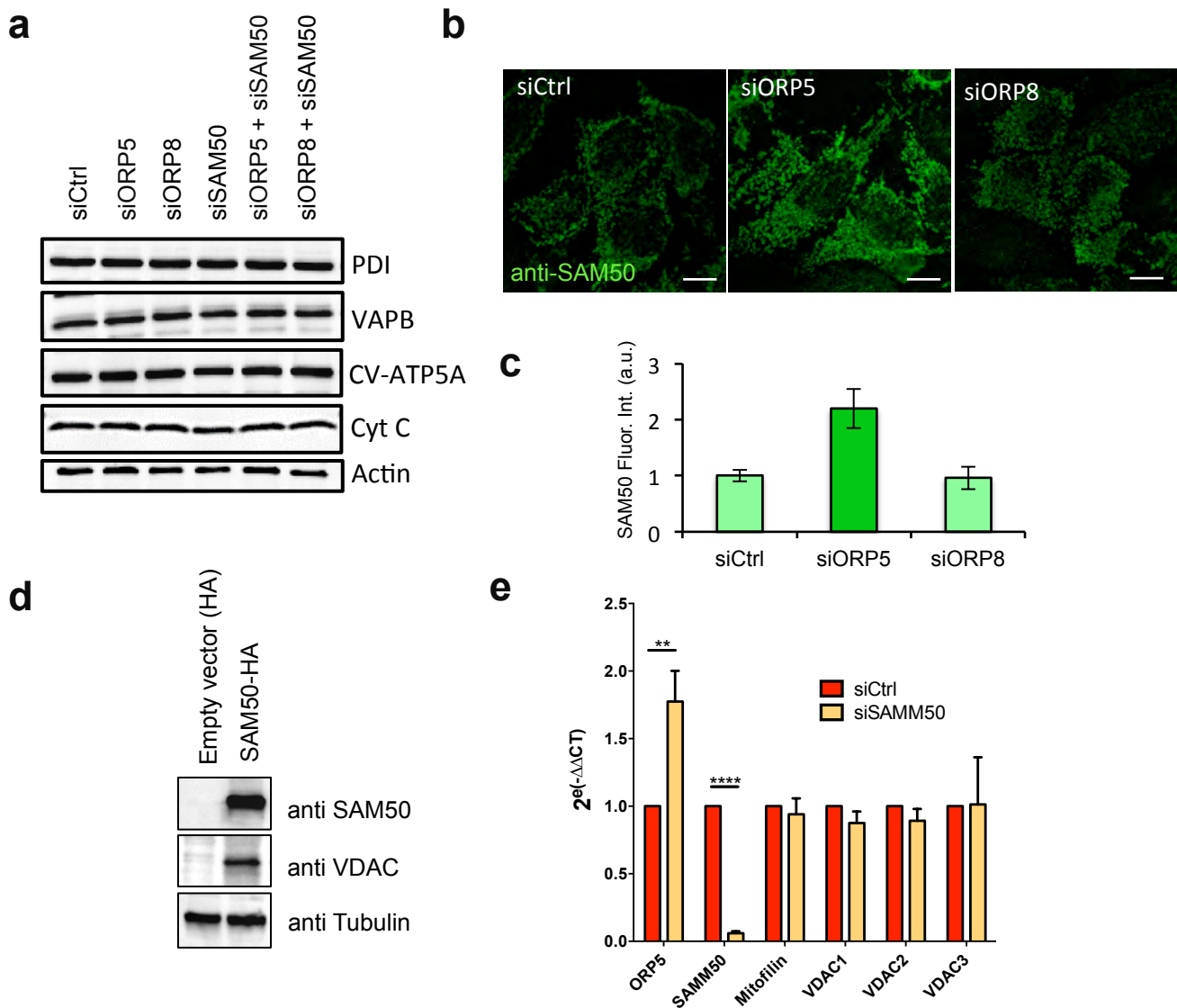**Figure S3.** (a-b) Confocal images of HeLa cell co-transfected with EGFP-ORP8 (a) or EGFP-ORP8ΔPH (b) (green) and SAM50-HA, immunostained with anti-HA to detect SAM50 (red). Insets show magnifications of the boxed regions. Scale bar, 10 μm.

Figure S3

Figure S4. (a) Representative EM micrographs showing the morphology of mitochondria in HeLa cells treated with siRNA against ORP5, ORP8, Mitofilin and SAM50. Scale bar, 200 nm. Red arrows indicate ER elements in contact with mitochondria; arrowheads indicate CJ; m, mitochondria. (b) Quantifications of the number of CJ per mitochondria profile in the indicated siRNA conditions. % of CJ ±SEM, n = 170-260 mitochondria, ***, p< 0.001; **, p< 0.01.

Figure S4

Figure S5. (a) WB analysis showing PDI (ER), VAPB (ER), CV-ATP5A (IMM), Cytochrome C (Cyt C, IMM) and Actin levels in protein lysates from HeLa cells treated with either Ctrl siRNAs or with siRNAs against ORP5, ORP8, or SAM50. (b) Confocal images of Ctrl, ORP5 and ORP8 knockdown HeLa cells immunostained using anti-SAM50 antibody (green). Scale bar, 10 µm. (c) Quantification of fluorescent intensity in SAM50-labelled cells. Normalized data from three independednt replicates are presented. Error bars denote ±SEM (d) WB analysis showing SAM50, VDAC and Tubulin levels in protein lysates from HeLa cells treated with either SAM50-HA or an empty vector. (e) Quantitative RT-PCR analysis of ORP5, SAM50, Mitofilin, VDAC1, VDAC2 and VDAC3 in SAM50 knockdown cells versus control HeLa cells. y axis: $2^{(-\Delta\Delta Ct)}$ value represents differences between the mean Ct (Cycle threshold) values of tested genes and those of reference gene (SDHA).

Figure S5

a

Mitochondrial membrane potential
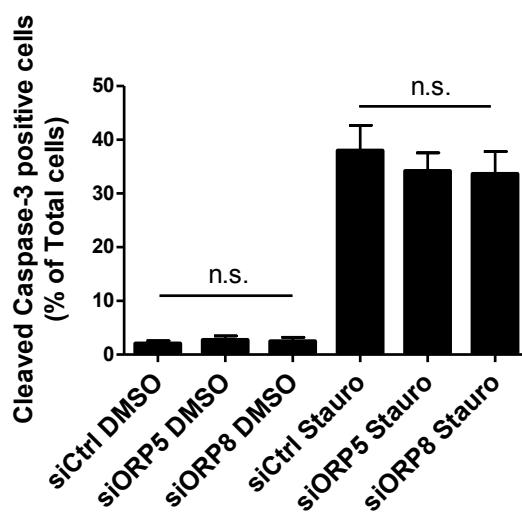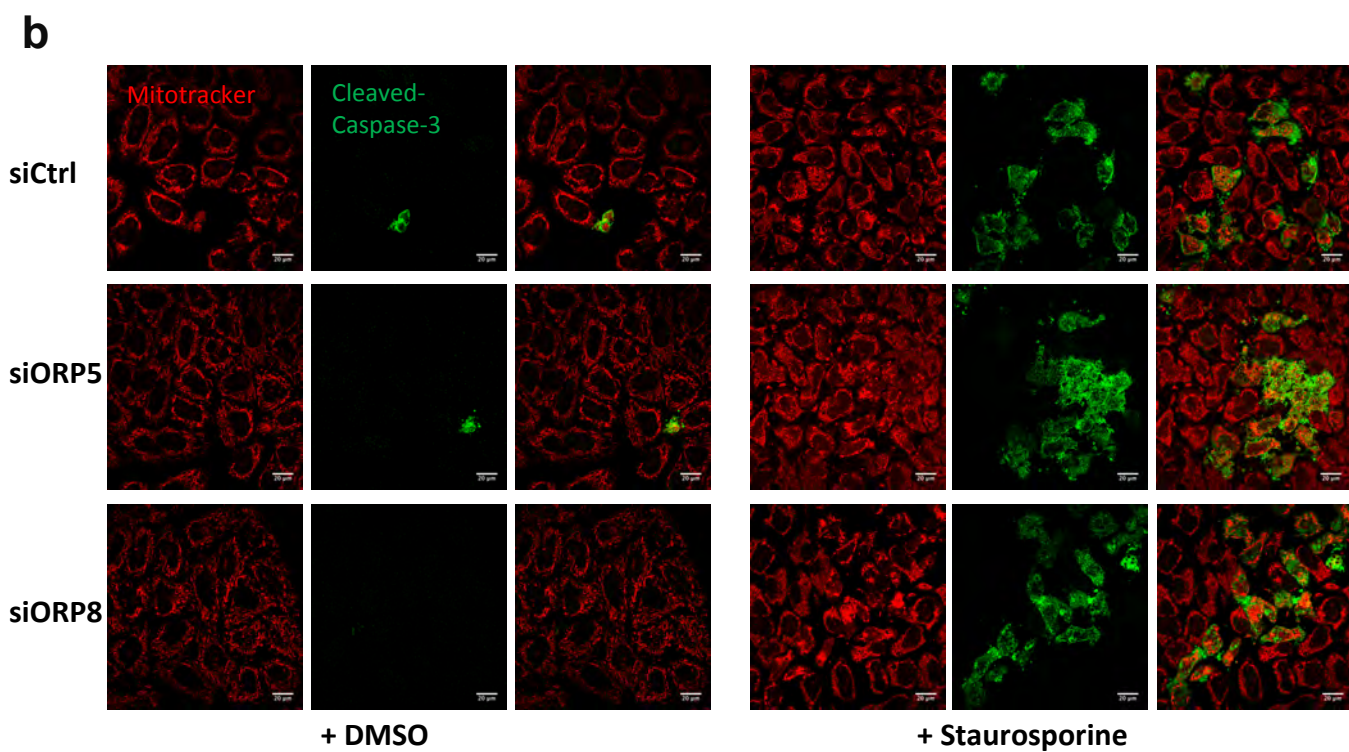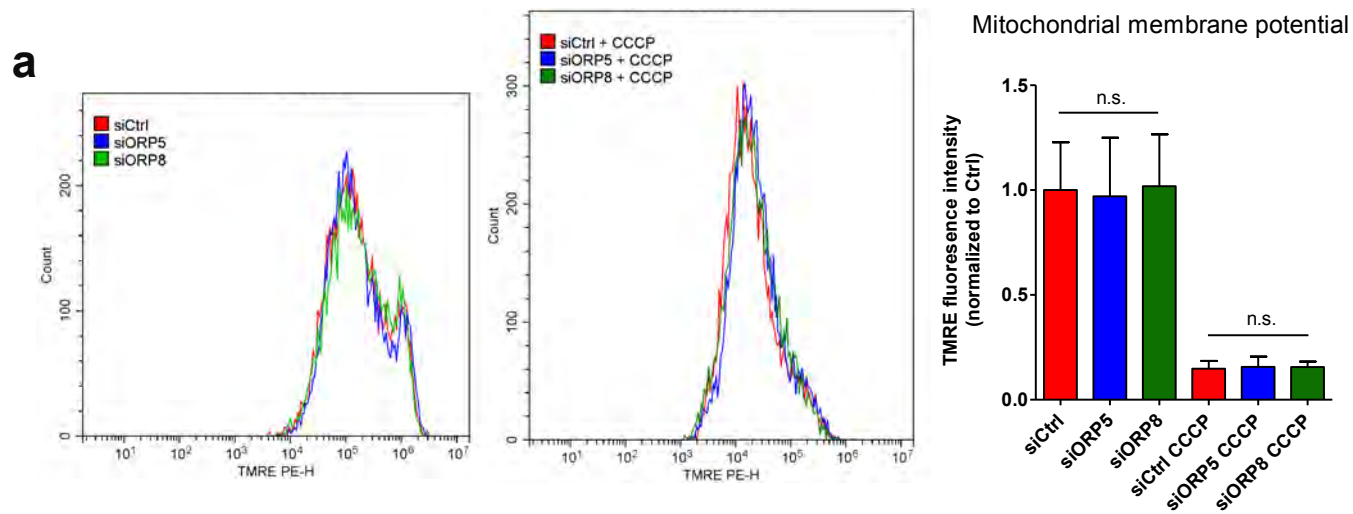
b

+ DMSO   + Staurosporine

Figure S6

Figure S6. (a) Representative graphs of flow cytometry analysis of HeLa cells transfected with siRNA against ORP5 or ORP8 (n = 10 000 cells) and loaded with the mitochondrial membrane potential sensitive dye TMRE, in presence (right graph) or absence (left graph) of CCCP. Flow cytometry histograms are showing the relative TMRE fluorescence intensity; the average of three independent replicates is shown. Data are presented as normalized mean ±SEM. (b) Fluorescent images of HeLa cells transfected with siRNA against ORP5, ORP8 or control, treated with DMSO or staurosporine and stained with anti-cleaved Caspase-3 (apoptotic cells) and Mitotracker. Scale bar, 20 μm. The graphs represent the means ±SEM of the percentage of cleaved Caspase-3 positive cells in the different conditions; the average of three independent replicates is shown, n.s; not significant.